Inorg. Chem. **2008**, *47*, 5394−5416

Variation of Average *g* Values and Effective Exchange Coupling Constants among [2Fe−2S] Clusters: A Density Functional Theory Study of the Impact of Localization (Trapping Forces) versus Delocalization (Double-Exchange) as Competing Factors

Maylis Orio and Jean-Marie Mouesca*

Laboratory of Inorganic and Biological Chemistry, CEA-INAC, 17 rue des Martyrs, 38054 Grenoble cedex 9, France

Received September 3, 2007

A phenomenological model aimed at rationalizing variations in both average **g**-tensor values ($g_{av} \equiv {}^1/_3\sum_i g_i$) and effective exchange coupling constants J_{eff} (defined as two-thirds of the energy difference between the $S = {}^3/_2$ and $S = {}^1/_2$ spin states) has been derived in order to describe the great variety of magnetic properties exhibited by reduced [2Fe−2S] clusters in proteins. The key quantity in the present analysis is the ratio $\Delta E/B$ computed from two competing terms. ΔE comprises various effects that result in trapping-site asymmetries: vibronic coupling and the chemical nature (S/N/O) and conformations of the ligands on the one hand and solvation terms, the hydrogen bonding network, etc., on the other. All of these additive terms (in a "bottom-up" approach) favor valence *localization* of the reducing electron onto one of the two iron sites. In contrast, the B term is the double-exchange term, which favors electronic *delocalization*. Both g_{av} and J_{eff} can be expressed as functions of $\Delta E/B$. We have also shown that electronic localization generally favors small g_{av} and large J_{eff} values (while the opposite is true for electronic delocalization) in a comparative study of the spectroscopic features of plant-type ferredoxins (Fd's) and Rieske centers (and related mutants). Two other types of problems were particularly challenging. The first of these involved deprotonated Rieske centers and the xanthine oxidase clusters II, which are characterized by very small J_{eff} values (40–45 cm^{-1} with a $J\hat{\mathbf{S}}_A \cdot \hat{\mathbf{S}}_B$ model) correlated with unusually large g_{av} values (in the range 1.97–2.01) as a result of an antisymmetric exchange coupling mechanism. The second concerned the analogous Fd's from *Clostridium pasteurianum* (Cp) and *Aquifex aeolicus* (Aa). Detailed Mössbauer studies of the C56S mutant of the Cp system revealed a mixture of clusters with valence-localized $S = {}^1/_2$ and valence-delocalized $S = {}^9/_2$ ground states. We relied on crystallographic structures of wild-type and mutant Aa Fd's in order to explain such a distribution of spin states.

Introduction

Iron−sulfur clusters constitute the active sites of an important class of metalloproteins that play an essential role in living beings.[1−6] They operate as electron carriers in electron-transfer chains and as reducing catalytic agents and are involved in such basic vital functions as photosynthesis, the respiratory chain, and nitrogen fixation. Among the many possible combinations of iron and sulfur atoms, let us first mention the $[1Fe](Cys)_4$ motif found in rubredoxins and desulforedoxins, in which the sulfur atoms form a weak pseudotetrahedral ligand field surrounding the high-spin iron ions.

* To whom correspondence should be addressed. E-mail: jean-marie.mouesca@cea.fr.

(1) Sykes, A. G.; Cammack, R. In *Advances in Inorganic Chemistry: Iron−Sulfur Proteins*; Sykes, A. G., Cammack, R., Eds.; Academic Press: London, 1999; Vol. *47*.
(2) Johnson, M. K. In *Encyclopedia of Inorganic Chemistry*; King, R. B., Ed.; Wiley: Chichester, England, 1994; Vol. *4*, p 1896.
(3) Lovenberg, W. In *Iron−Sulfur Proteins, Volume III: Storage and Metabolic Mechanisms*; Lovenberg, W., Ed.; Academic Press: New York, 1977.
(4) Lovenberg, W. In *Iron−Sulfur Proteins, Volume II: Molecular Properties*; Lovenberg, W., Ed.; Academic Press: New York, 1973.
(5) Lovenberg, W. In *Iron−Sulfur Proteins, Volume I: Biological Principles*; Lovenberg, W., Ed.; Academic Press: New York, 1973.
(6) Link, T. A. In *Advances in Inorganic Chemistry: Iron−Sulfur Proteins*; Sykes, A. G., Cammack, R., Eds.; Academic Press: London, 1999; Vol. *47*, p 83.

10.1021/ic701730h CCC: $40.75
Published on Web 05/21/2008

Next in terms of complexity come the [2Fe−2S](Cys)$_4$ clusters, which are found in plant-, vertebrate-, and bacterial-type ferredoxins (Fd's)[2,7,8] in the thioredoxin-like family,[9] as well as the [2Fe−2S](Cys)$_2$(His)$_2$ groups present in Rieske-type centers.[10–12] These two families (and related mutants)[13–15] were the main focus of the present work. They represent the simplest examples of spin-coupled systems, in which the total cluster spin is $\mathbf{S} = \mathbf{S_A} + \mathbf{S_B}$, where A and B label the two iron centers. Dominant superexchange mechanisms mediated by the sulfide bridges are described by a Heisenberg spin Hamiltonian of the form $\hat{H}_{\text{Heis}} = J_{\text{Heis}}\hat{\mathbf{S}}_{\text{A}}\cdot\hat{\mathbf{S}}_{\text{B}}$, resulting in a low-spin $S = 0$ antiferromagnetic ground state, as commonly observed for the oxidized [Fe^{3+}−Fe^{3+}] redox state.

In the reduced state, the Heisenberg formalism presupposes full electronic localization of the reducing electron on one of the two iron sites (to give [Fe^{2+}−Fe^{3+}] or [Fe^{3+}−Fe^{2+}]), resulting in a $S = {}^1/_2$ antiferromagnetic ground state. A double-exchange mechanism that favors electronic delocalization through mixing of the [Fe^{3+}−Fe^{2+}] ("a") and [Fe^{2+}−Fe^{3+}] ("b") configurations is also operative.[16,17] In the case of full electronic delocalization [$Fe^{2.5+}$−$Fe^{2.5+}$] (i.e., with equivalent site energies $E_a \approx E_b$), the double-exchange energy contribution to the spin Hamiltonian is written as $\pm B(S + {}^1/_2)$,[18–21] where B is proportional to the $\langle d_{z^2A}|d_{z^2B}\rangle$ orbital overlap integral (with the Fe−Fe axis along z). In a very few instances, this double-exchange term becomes dominant over the Heisenberg term and leads to the rarely observed $S = {}^9/_2$ high-spin state.[15,22,23]

Finally, in addition to these competing localizing (J_{Heis}) and delocalizing (B) exchange-only effects, a third key player is essential for a proper understanding of the electronic and magnetic properties of the [2Fe−2S] clusters. The trapping term[24–26] $\Delta E = (E_b - E_a)/2$ can be decomposed into $\Delta E = \Delta E_{\text{in}} + \Delta E_{\text{out}}$ (where "in" denotes "inside/intrinsic" and "out" stands for "outside/extrinsic"). The first term, ΔE_{in}, comprises contributions from within the cluster: (i) the (static) ligand chemical asymmetry (ΔE_{chem}) (as in Rieske centers), (ii) ligand conformations and orientations (ΔE_{Ω}), and (iii) (dynamic) vibronic effects (ΔE_{vib}).[27–29] The second term, ΔE_{out}, contains contributions induced by the near and far cluster environment: (i) solvent proximity or accessibility (ΔE_{solv}), (ii) the differential hydrogen bond network around the cluster (ΔE_{H}), and (iii) other contributions, such as the global electrostatic potential originating in the protein charge distribution.

A nonzero ΔE term results in partial or total charge trapping and counteracts the delocalizing double-exchange B term. Therefore, the key quantity is the ratio $\Delta E/B$. In the total spin Hamiltonian of the system and the resulting expressions for the spin-state energies ε_S, ΔE and B are combined in a way that permits the derivation of expressions for the average value of the **g**-tensor components [$g_{\text{av}} \equiv (g_1 + g_2 + g_3)/3$, where $g_1 > g_2 > g_3$] and the effective exchange coupling constant [$J_{\text{eff}} \equiv {}^2/_3(\varepsilon_{3/2} - \varepsilon_{1/2})$] as functions of $\Delta E/B$ (see Theoretical Model, below). In the case of J_{eff}, when ΔE is restricted to its vibronic contribution ΔE_{vib}, it is known[24,26,30] that a ferromagnetic contribution J_{Ferro} (which is a function of $\Delta E_{\text{vib}}/B$) must be added to the Heisenberg exchange coupling constant J_{Heis}, yielding $J_{\text{eff}} = J_{\text{Heis}} + J_{\text{Ferro}}$. In this work, we will show how experimental g_{av} and J_{eff} values may be correlated through $\Delta E/B$.

In the present paper, we have chosen to set aside more complicated systems (containing three or more spin-coupled Fe atoms) in favor of an extensive study of the simpler [2Fe−2S] class (ferredoxins and Rieske-type systems), with the hope of illustrating as clearly as possible the issues already involved at this level.

[2Fe−2S] Ferredoxins versus Rieske Proteins. The interplay between J_{Heis}, B, and ΔE terms results in finely tuned electronic and magnetic properties that can be revealed and measured using electronic and magnetic resonance spectroscopy methods: electronic paramagnetic resonance (EPR), which yields **g** tensors,[31–34] nuclear magnetic reso-

(7) Mitou, G.; Higgins, C.; Wittung-Stafshede, P.; Conover, R. C.; Smith, A. D.; Johnson, M. K.; Gaillard, J.; Stubna, A.; Münck, E.; Meyer, J. *Biochemistry* **2003**, *42*, 1354.
(8) Holden, H. M.; Jacobson, B. L.; Hurley, J. K.; Tollin, G.; Oh, B. H.; Skjeldal, L.; Chae, Y. K.; Cheng, H.; Xia, B.; Markley, J. L. *J. Bioenerg. Biomembr.* **1994**, *26*, 67.
(9) Meyer, J. *FEBS Lett.* **2001**, *509*, 1.
(10) Schneider, D.; Schmidt, C. L. *Biochim. Biophys. Acta* **2005**, *1710*, 1.
(11) Lebrun, E.; Santini, J.-M.; Brugna, M.; Ducluzeau, A.-L.; Ouchane, S.; Schoepp-Cothenet, B.; Baymann, F.; Nitschke, W. *Mol. Biol. Evol.* **2006**, *23*, 1180.
(12) Hunsicker, L. M.; Heine, A.; Chen, Y.; Luna, E. P.; Todaro, T.; Zhang, Y. M.; Williams, P. A.; McRee, D. E.; Hirst, J.; Stout, D.; Fee, J. A. *Biochemistry* **2003**, *42*, 7303.
(13) Kounosu, A.; Li, Z.; Cosper, N. J.; Shokes, J. E.; Scott, R. A.; Imai, T.; Urushiyama, A.; Iwasaki, T. *J. Biol. Chem.* **2004**, *279*, 12519.
(14) Hurley, J. K.; Weber-Main, A. M.; Hodges, A. E.; Stankovich, M. T.; Benning, M. M.; Holden, H. M.; Cheng, H.; Xia, B.; Markley, J. L.; Genzor, C.; Gomez-Moreno, C.; Hafezi, R.; Tollin, G. *Biochemistry* **1997**, *36*, 15109.
(15) Achim, C.; Bominaar, E. L.; Meyer, J.; Peterson, J.; Münck, E. *J. Am. Chem. Soc.* **1999**, *121*, 3704.
(16) Noodleman, L.; Norman, J. G.; Osborne, J. H. J.; Aizman, A.; Case, D. A. *J. Am. Chem. Soc.* **1985**, *107*, 3418.
(17) Noodleman, L.; Baerends, E. J. *J. Am. Chem. Soc.* **1984**, *106*, 2316.
(18) Zener, C. *Phys. Rev.* **1951**, *82*, 403.
(19) Anderson, P. W.; Hasegawa, H. *Phys. Rev.* **1955**, *100*, 675.
(20) Papaefthymiou, G. C.; Girerd, J.-J.; Moura, I.; Moura, J. J. G.; Münck, E. *J. Am. Chem. Soc.* **1987**, *109*, 4703.
(21) Münck, E.; Papaefthymiou, G. C.; Surerus, K. K.; Girerd, J.-J.; Que, L. *ACS Symp. Ser.* **1988**, *372*, 4703.
(22) Crouse, B. R.; Meyer, J.; Johnson, M. K. *J. Am. Chem. Soc.* **1995**, *117*, 9612.
(23) Achim, C.; Golinelli, M. P.; Bominaar, E. L.; Meyer, J.; Münck, E. *J. Am. Chem. Soc.* **1996**, *118*, 8168.
(24) Noodleman, L.; Case, D. A.; Mouesca, J.-M.; Lamotte, B. *J. Biol. Inorg. Chem.* **1996**, *1*, 177.
(25) Ding, X.-Q.; Bill, E.; Trautwein, A. X.; Winkler, H. *J. Chem. Phys.* **1993**, *99*, 6421.
(26) Blondin, G.; Girerd, J.-J. *Chem. Rev.* **1990**, *90*, 1359.
(27) Piepho, S. B.; Krausz, E. R.; Schatz, P. N. *J. Am. Chem. Soc.* **1978**, *100*, 2996.
(28) Piepho, S. B. *J. Am. Chem. Soc.* **1988**, *110*, 6319.
(29) Girerd, J.-J. *J. Chem. Phys.* **1983**, *79*, 1766.
(30) Bominaar, E. L.; Borshch, S. A.; Girerd, J.-J. *J. Am. Chem. Soc.* **1994**, *116*, 5362.
(31) Wegner, P.; Bever, M.; Schunemann, V.; Trautwein, A. X.; Schmidt, C.; Bönish, H.; Gnida, M.; Meyer-Klaucke, W. *Hyperfine Interact.* **2004**, *158*, 293.
(32) Le Pape, L.; Lamotte, B.; Mouesca, J.-M.; Rius, G. *J. Am. Chem. Soc.* **1997**, *119*, 9757.
(33) Hagen, W. R. In *Cytochrome Systems. Molecular Biology and Bioenergetics*; Papa, S., Chance, B., Ernster, L., Eds.; Plenum Press: New York, 1987; p 459.
(34) Guigliarelli, B.; Bertrand, P. *Adv. Inorg. Chem.* **1999**, *47*, 421–497.

nance (NMR), which yields chemical shifts/tensors,[35–38] and electron–nuclear double resonance (ENDOR), which yields hyperfine tensors.[39–42] In addition, Mössbauer techniques (to obtain quadrupole splittings and isomer shifts)[31,43–45] as well as other methods can be employed. Among the various spectroscopic observables, we have focused our interest and efforts on the **g** tensors measured by EPR techniques.

The three types of [2Fe−2S] ferredoxins (plant, vertebrate/bacterial, and thioredoxin-like) are characterized by a g_{av} value of 1.96. In order to rationalize the distribution of values of the three **g**-tensor components $\{g_i\}$, which range from rhombic values (typically $g_1 \approx 2.04$, $g_2 \approx 1.96$, and $g_3 \approx 1.88$ for plant-type Fd's) to axial values ($g_1 \approx 2.02$ and $g_2 \approx g_3 \approx 1.94$ for vertebrate-type Fd's), Bertrand and Gayda[34,46,47] devised a phenomenological model linking the observed magnetostructural correlations (plots of $\{g_i\}$ as a function of $g_2 - g_3$) to the relative weights of the d_{z^2} and $d_{x^2-y^2}$ orbitals in Ψ_0, the sixth d molecular orbital (MO) of the ferrous ion. Recently,[48] a density functional theory (DFT) study based on crystallographic structures of plant-type [2Fe−2S] proteins improved that model by computing the effect of the cysteine ligand orientations (expressed in terms of Fe−Fe−S−C dihedral angles) on the variation of the three **g**-tensor components.

On the other hand, Rieske centers can be classified in three main groups.[10–12] The first group contains the (high-potential) Rieske proteins present in many photosynthetic or respiratory electron-transfer chains of all three kingdoms of life (bacterial/archaeal). The second group encompasses the (low-potential) so-called "Rieske-type" proteins such as the bacterial dioxygenases. Finally, a third and more heterogeneous group comprises Rieske proteins having intermediate potentials, such as the arsenite oxidases and the (bc_1-type) Rieske protein from *Thermus thermophilus*.

The group led by Bertrand[46] later applied their phenomenological analysis to Rieske-type proteins (having typical $\{g_i\}$ values of 1.80, 1.90, and 2.02 at pH 7) as well as to a selection of synthetic [2Fe−2S] complexes in their reduced states; both sets were characterized by a common g_{av} value of 1.91. The ferrous ion in the Rieske clusters is located on the histidine side.

Table 1. Values of g_{av} for [2Fe−2S] Active Sites

system	ligands[a]	g_1	g_2	g_3	g_{av}
1CZP[b] WT Fd	$(C_2)(C_2)$	2.05	1.96	1.88	1.96
1CZP[b] (C41S)	$(SC)(C_2)$	2.02	1.91	1.82	1.917
1CZP[b] (C46S)	$(CS)(C_2)$	2.02	1.95	1.89	1.953
1QOA[b,c] (C49S)	$(C_2)(SC)$	2.02	1.92	1.90	1.947
1CZP[b] (C79S)	$(C_2)(CS)$	2.03	1.93	1.89	1.950
1XLQ[d] WT Fd	$(C_2)(C_2)$	2.02	1.940	1.940	1.96
1M2A[e] WT	$(C_2)(C_2)$	2.004	1.948	1.922	1.958
1M2B[e] (C56S)	$(SC)(C_2)$	2.007	1.916	1.883	1.935
1M2D[e] (C60S)	$(CS)(C_2)$	2.005	1.923	1.882	1.937
XO[f] clusters I	$(C_2)(C_2)$	2.01–2.04	1.93–1.95	1.89–1.92	1.95–1.97
XO[f] clusters II	$(C_2)(C_2)$	2.06–2.16	1.97–2.01	1.87–1.92	1.97–2.01
Rieske[g] pH 7	$(H_2)(C_2)$	2.02	1.90	1.81	1.91
Rieske[h] (H64C)	$(HC)(C_2)$	2.00	1.92	1.92	1.947
Rieske[i] pH 14	$((H\text{-deprot})_2)(C_2)$	2.14	1.94	1.81	1.97

[a] C = Cys, S = Ser, and H = His. [b] Crystal structure in the reduced state of the WT cyanobacterial ferredoxin of *Anabaena* (PDB entry 1CZP);[49] EPR spectral *g* values for WT and related mutants.[14,50] [c] Crystal structure in the oxidized state of the C49S mutant of the cyanobacterial ferredoxin of *Anabaena* (PDB entry 1QOA).[14] [d] Crystal structure of the reduced C73S putidaredoxin from *P. putida* (PDB entry 1XLQ).[51] [e] Crystal structures of WT and mutant ferredoxins from *A. aeolicus* (PDB entries 1M2A, 1M2B, and 1M2D, respectively);[52] EPR spectral *g* values given for the analogous ferredoxin from *C. pasteurianum* for WT and related mutants.[53,54] [f] EPR spectral *g* values from ref 55. [g] EPR spectral *g* values from refs 34 and 46. [h] EPR spectral *g* values from ref 13. [i] EPR spectral *g* values from ref 56.

We have focused our efforts on these g_{av} values for as many different systems as possible, in order to quantify the impact of the chemical nature (N vs S) and conformation of the ligands as well as that of the environment (solvent, etc.).

Mutant and Altered Forms. The Rieske-type [2Fe−2S] cluster from *Sulfolobus solfataricus*[13] in its reduced state ($g_{av} \approx 1.91$; see Table 1) has been mutated (in its oxidized form) into a $(Cys)_3(His)$ cluster. After further reduction by the dithionite, this H64C (unstable) mutant showed a nearly axial EPR signal at $g_1 \approx 2.00$ and $g_2 \approx g_3 \approx 1.92$, that is, at $g_{av} \approx 1.947$. Not surprisingly, this last value is intermediate between those for $(Cys)_2(His)_2$ and $(Cys)_4$ (1.91 and 1.96, respectively).

Among the four mutants (Cys → Ser) of the plant-type Fd from the cyanobacterium *Anabaena* (see Table 1), one (C41S) exhibits a g_{av} value (1.917) that is smaller than the three others (1.953, 1.947, and 1.950 for C46S, C49S, and C79S, respectively). In the wild type (WT), the reduced iron site is the one closest to the protein surface (Fe#1, bearing Cys41 and Cys46); this fact is not altered by any of the four Cys → Ser mutations, as concluded from NMR studies.[50]

Similar studies have been performed for the bacterial-type Fd from *Clostridium pasteurianum* (Cp) with serine-mutated

(35) Crozet, M.; Chaussade, M.; Bardet, M.; Emsley, L.; Lamotte, B.; Mouesca, J.-M. *J. Phys. Chem. A* **2000**, *104*, 9990.
(36) Ciurli, S.; Cremonini, M. A.; Kofod, P.; Luchinat, C. *Eur. J. Biochem.* **1996**, *236*, 405.
(37) Cheng, H.; Markley, J. L. *Annu. Rev. Biophys. Biomol. Struct.* **1995**, *24*, 209.
(38) Bertini, I.; Capozzi, F.; Luchinat, C.; Piccioli, M. *Eur. J. Biochem.* **1993**, *212*, 69.
(39) Mouesca, J.-M.; Rius, G.; Lamotte, B. In *Mixed Valency Systems: Applications in Chemistry, Physics and Biology*; Prassides, K., Ed.; Kluwer Academic Publishers: Dordrecht, The Netherlands, 1991; p 431.
(40) Moriaud, F.; Gambarelli, S.; Lamotte, B.; Mouesca, J.-M. *J. Phys. Chem. B* **2001**, *105*, 9631.
(41) Le Pape, L.; Lamotte, B.; Mouesca, J.-M.; Rius, G. *J. Am. Chem. Soc.* **1997**, *119*, 9771.
(42) Hoffman, B. M. *Proc. Natl. Acad. Sci. U.S.A.* **2003**, *100*, 3575.
(43) Trautwein, A. X.; Bill, E.; Bominaar, E. L.; Winkler, H. *Struct. Bonding (Berlin)* **1991**, *78*, 1.
(44) Schünemann, V.; Winkler, H. *Rep. Prog. Phys.* **2000**, *63*, 263.
(45) Beinert, H.; Holm, R. H.; Münck, E. *Science* **1997**, *277*, 653.
(46) Bertrand, P.; Guigliarelli, B.; Gayda, J.-P.; Beardwood, P.; Gibson, J. F. *Biochim. Biophys. Acta* **1985**, *831*, 261.
(47) Bertrand, P.; Gayda, J.-P. *Biochim. Biophys. Acta* **1979**, *579*, 107.
(48) Gambarelli, S.; Mouesca, J.-M. *Inorg. Chem.* **2004**, *43*, 1441.
(49) Morales, R.; Chron, M.-H.; Hudry-Clergeon, G.; Pétillot, Y.; Norager, S.; Medina, M.; Frey, M. *Biochemistry* **1999**, *38*, 15764.
(50) Cheng, H.; Xia, B.; Reed, G. H.; Markley, J. L. *Biochemistry* **1994**, *33*, 3155.
(51) Sevrioukova, I. F. *J. Mol. Biol.* **2005**, *347*, 607.
(52) Yeh, A. P.; Ambroggio, X. L.; Andrade, S. L. A.; Einsle, O.; Chatelet, C.; Meyer, J.; Rees, D. C. *J. Biol. Chem.* **2002**, *277*, 34499.
(53) Meyer, J.; Fujinaga, J.; Gaillard, J.; Lutz, M. *Biochemistry* **1994**, *33*, 13642.
(54) Fijinaga, J.; Gaillard, J.; Meyer, J. *Biochem. Biophys. Res. Commun.* **1993**, *194*, 104.

ligands.[15,22,23,53,54] The WT protein has $g_1 \approx 2.00$, $g_2 \approx 1.95$, and $g_3 \approx 1.92$ ($g_{av} \approx 1.96$), whereas two of the Cys → Ser mutants, C56S and C60S, exhibit nearly identical g_{av} values (1.935 and 1.937, respectively). These values again fall between 1.91 and 1.96. No crystallographic structures are available for either the reduced WT Cp Fd or its mutated forms. However, high-resolution structures of the oxidized Fd from the similar bacterium *Aquifex aeolicus* (Aa) and its C55S and C59S mutants (counterparts of the C56S and C60S Cp mutants) have been obtained. Our subsequent analysis was based on these structures. In addition, a rare and very exciting feature of the Cp Fd mutants is that they both exhibit a mixture of clusters having either $S = {}^1/_2$ or $S = {}^9/_2$ spin states in the ground state.[15,23] We therefore must explain how chemical ligand asymmetry, (Cys)(Ser) versus $(Cys)_2$, is efficiently counteracted by valence delocalization, which is a priori a counter-intuitive statement. We will return to this point in more detail as we search for the origin of such a striking feature.

Rieske Protein at pH 14 and Xanthine Oxidase Family. Recently, a very large g_{av} value (∼1.97) was measured for the reduced *T. thermophilus* (Tt) Rieske protein at pH 14. de Oliveira et al.[56] explained the occurrence of the highly anisotropic g_i values (1.81, 1.94, and 2.14) and line widths in the Tt Rieske protein by adding an extra antisymmetric exchange term[57] of the form $\mathbf{d}_{AB}\cdot\hat{\mathbf{S}}_A \times \hat{\mathbf{S}}_B$ that mixes the $M_S = \pm{}^3/_2$ states of the $S = {}^3/_2$ excited state into the $S = {}^1/_2$ ground state. The fit of the temperature dependence of the EPR signal yielded $J_{eff} \approx 43$ cm^{-1}. In contrast, J_{eff} values for protonated reduced Rieske centers are typically between 130 and 380 cm^{-1}.[58–60]

Finally, it has been noticed by de Oliveira et al.[56] that the unusually large $\{g_i\}$ values and line widths observed for the Tt Rieske protein at pH 14 are very similar to those reported for signal II of the xanthine oxidase (XO) class.[55] The proteins of the XO group contain two [2Fe−2S](Cys)$_4$ clusters, yielding two EPR signals (I and II) that are assigned using the temperature dependence of the EPR signal from the Mo(V) center.[55] The cluster that yields signal I is deeply buried within the protein matrix and is analogous to the standard plant-type Fd's in terms of **g**-tensor component values ($g_{av} \approx 1.96$). The second cluster, which yields signal II and is located near the protein surface, is unusual in that the g_{av} values range from 1.97 to 2.01, with g_1 values of 2.06−2.16 (compared to 2.01–2.05 for XO signal I and plant-type Fd's). It should be noted that clusters II (yielding $J_{eff} \approx 40$ cm^{-1})[55] are solvent-exposed and structurally very similar to the plant-type Fd clusters, which exhibit significantly larger J_{eff} values (in the 120–150 cm^{-1} range; see refs 58, 61, and 62and references therein), whereas clusters I, which are deeply buried and present unusual geometries, are characterized by standard g_{av} values (∼1.96).

Goals Pursued in This Work. In the present DFT study, we have aimed at illustrating as simply as possible and in a semiquantitative way the various effects that can affect g_{av} values of [2Fe−2S] cluster, which range from 1.91 to 2.01, in order to offer a sufficiently broad and unified view rationalizing such a great variability. To summarize the essence of our analysis, an electronically *delocalized* system exhibits a larger g_{av} value, whereas an electronically *localized* system exhibits a smaller g_{av} value. This is the basic difference between plant-type ferredoxins with chemically symmetric ligands ($g_{av} \approx 1.96$) and Rieske centers presenting His-versus-Cys chemical asymmetry ($g_{av} \approx 1.91$). In order to treat these two cases and situations in between (i.e., involving mutants), we must estimate the magnitudes of the various trapping forces, ΔE. We tackled all of these issues by computing both high-spin ($S = {}^9/_2$) and broken-symmetry ($M_S = {}^1/_2$) states (see Methodology, below).

The $\Delta E/B$ ratio served as a common and practical index, allowing us to compare and classify the electronic structures [delocalized (class III), localized (class I), or in-between (class II), using the classification scheme of Robin and Day[63]] of the various [2Fe−2S] systems and related model molecules and to rationalize the resulting distribution of g_{av} values within a common conceptual framework. Two drawbacks must be kept in mind, however. First, the computed $\Delta E/B$ ratio is obviously model-dependent [i.e., dependent on the choice of ligands and environment (protein matrix and/or solvent, hydrogen bonds, etc)]. Second, it depends on the exchange correlation (XC) potential used. Therefore, we have focused our interest on relative $\Delta E/B$ ratios for a given XC potential rather than on absolute values as such. Therefore, our approach is phenomenological.

Theoretical Model

A. Phenomenological Approach: Electronic Delocalization versus Trapping Forces. In this introductory discussion about the interplay between delocalization and trapping forces, let Ψ_a and Ψ_b (where "a" denotes [Fe^{3+}−Fe^{2+}] and "b" signifies [Fe^{2+}−Fe^{3+}]) be the configurations corresponding to energies E_a and E_b, respectively. We first consider a phenomenological description of the issues involved and then explicitly treat dynamic (i.e., vibronic) and static [i.e., electrostatic (ligand nature, orientation) and solvent (dielectric continuum)] terms in E_a and E_b. The eigenvalue problem can be expressed as[25]

(55) Caldeira, J.; Belle, V.; Asso, M.; Guigliarelli, B.; Moura, I.; Moura, J. G. J.; Bertrand, P. *Biochemistry* **2000**, *39*, 2700.
(56) de Oliveira, F. T.; Bominaar, E. L.; Hirst, J.; Fee, J. A.; Münck, E. *J. Am. Chem. Soc.* **2004**, *126*, 5338.
(57) Bencini, A.; Gatteschi, D. In *EPR of Exchange Coupled Systems*; Springer-Verlag: Berlin, 1990.
(58) Bertrand, P.; Gayda, J.-P.; Fee, J. A.; Kuila, D.; Cammack, R. *Biochim. Biophys. Acta* **1987**, *916*, 24.
(59) Leggate, E. J.; Bill, E.; Essigke, T.; Ullmann, G. M.; Hirst, J. *Proc. Natl. Acad. Sci. U.S.A.* **2004**, *101*, 10913.
(60) Salerno, J. C.; Ohnishi, T.; Blum, H.; Leigh, J. S. *Biochim. Biophys. Acta* **1977**, *494*, 191.
(61) Lloyd, S. G.; Franco, R.; Moura, J. J. G.; Moura, I.; Ferreira, G. C.; Huynh, B. H. *J. Am. Chem. Soc.* **1996**, *118*, 9892.
(62) Beardwood, P.; Gibson, J. F. *J. Chem. Soc., Dalton Trans.* **1983**, 737.
(63) Robin, M. B.; Day, P. *Adv. Inorg. Chem. Radiochem.* **1967**, *10*, 247.

$$\begin{bmatrix} \left(\frac{J_{\text{Heis}}}{2}\right)S(S+1)+E_{\text{a}} & -E_B(S) \\ -E_B(S) & \left(\frac{J_{\text{Heis}}}{2}\right)S(S+1)+E_{\text{b}} \end{bmatrix}\begin{pmatrix}\Psi_{\text{a}}\\ \Psi_{\text{b}}\end{pmatrix}=\varepsilon_S\begin{pmatrix}\Psi_{\text{a}}\\ \Psi_{\text{b}}\end{pmatrix} \tag{1}$$

In eq 1, J_{Heis} refers to the exchange coupling constant describing the Heisenberg (i.e., valence-localized) magnetic spin states and $E_B(S) = B(S + {}^1/_2)$ is the double-exchange term. Later in this section, we will come back to the computation of J_{Heis}. The two roots of eq 1, denoted $\varepsilon_S(\pm)$, are

$$\varepsilon_S(\pm)=\left(\frac{E_{\text{a}}+E_{\text{b}}}{2}\right)+\left(\frac{J_{\text{Heis}}}{2}\right)S(S+1)\pm\sqrt{\Delta E^2+B^2(S+{}^1/_2)^2} \tag{2}$$

where $\Delta E = (E_{\text{b}} - E_{\text{a}})/2$. The eigenfunctions are expressed as $c_{\text{a}}(S)\Psi_{\text{a}} \pm c_{\text{b}}(S)\Psi_{\text{b}}$. For a given spin state S, the coefficients $c_{\text{a}}(S)$ and $c_{\text{b}}(S)$ corresponding to the lower-energy eigenvalue $\varepsilon_S(-)$ depend on the ratio $\phi_S = \Delta E/[B(S + {}^1/_2)]$:

$$c_{\text{a}}(S)=\frac{\phi_S+\sqrt{1+\phi_S{}^2}}{\sqrt{1+\left(\phi_S+\sqrt{1+\phi_S{}^2}\right)^2}}$$
$$c_{\text{b}}(S)=\frac{1}{\sqrt{1+\left(\phi_S+\sqrt{1+\phi_S{}^2}\right)^2}} \tag{3}$$

The coefficients $c_{\text{a}}({}^9/_2)$ and $c_{\text{b}}({}^9/_2)$ can be extracted from the highest occupied molecular orbital (HOMO) bearing the reducing electron in the high-spin (HS) ($S = {}^9/_2$) state (see Scheme 1). The gap $\Delta\varepsilon_S = \varepsilon_S(+) - \varepsilon_S(-)$ between the (+) and (−) eigenvalues, the intervalence (metal-to-metal) band, is expressed as

$$\Delta\varepsilon_S=2\sqrt{\Delta E^2+B^2(S+{}^1/_2)^2} \tag{4}$$

The gap $\Delta\varepsilon_{9/2}$ can be computed from the same HS ($S = {}^9/_2$) spin state by applying the Slater transition-state procedure[64] to the bonding and antibonding MOs that are mainly linear combinations of d_{z^2A} and d_{z^2B}. Combining eqs 3 and 4 (with $\phi_{9/2} = \Delta E/5B$) gives

$$B=\frac{\Delta\varepsilon_{9/2}}{10\sqrt{1+\phi_{9/2}{}^2}} \quad \text{and} \quad \Delta E=\frac{\Delta\varepsilon_{9/2}}{2\sqrt{1+(1/\phi_{9/2}{}^2)}} \tag{5}$$

Finally, one can reconstruct the wave function of the partially localized/delocalized $S = {}^1/_2$ spin state using eq 3. It can be verified that for a given value of the $\Delta E/B$ ratio, the $S = {}^1/_2$ state is intrinsically more localized than the corresponding HS state [i.e., $c_{\text{a}}({}^1/_2) > c_{\text{a}}({}^9/_2)$]. Moreover, for large values of the $\Delta E/B$ ratio, $c_{\text{a}}({}^1/_2) \rightarrow 1$ and $c_{\text{b}}({}^1/_2) \rightarrow 0$, and one reaches the (Heisenberg) localized limit Ψ_{a} (the $[Fe^{3+}-Fe^{2+}]$ configuration only).

Exchange Coupling Constants. As already stated in the Introduction, the [2Fe−2S] species can be seen as two high-spin rubredoxin-like iron monomers (A and B) experiencing a weak (i.e., superexchange) interaction ($\hat{H}_{\text{Heis}} = J_{\text{Heis}}\hat{\mathbf{S}}_{\text{A}}\cdot\hat{\mathbf{S}}_{\text{B}}$ throughout). The first biologically relevant form of the [2Fe−2S] species is the oxidized cluster $[Fe^{3+}-Fe^{3+}]$, for which only $\hat{H}_{\text{Heis}}$ is operative, resulting in an $S = 0$ ground spin state. From the computation of the HS ($S = 5$) state and the broken-symmetry (BS) ($M_S = 0$) state (a mixture of the $M_S = 0$ components of all of the pure spin states $S = 0$ to $S = 5$), one can derive an expression linking $J_{\text{Heis}}(\text{ox})$ to the DFT spin-state energies $E^{\text{HS}}(\text{ox})$ and $E^{\text{BS}}(\text{ox})$. Using spin-projection techniques[16,17,65,66] (with $S_{\text{A}} = S_{\text{B}} = {}^5/_2$), we have

$$J_{\text{Heis}}(\text{ox})=\frac{E^{\text{HS}}(\text{ox})-E^{\text{BS}}(\text{ox})}{2S_{\text{A}}S_{\text{B}}} \tag{6}$$

with $2S_{\text{A}}S_{\text{B}} = 25/2$. In the corresponding nonprojected approach,[67,68] the denominator in eq 6 is replaced by $(2S_{\text{A}}S_{\text{B}} + S_{\text{B}})$. The two expressions differ by only 20% for Fe(III), while for Cu(II) dimers, they differ by a factor 2. In the following, we will present spin-projected results. However, the equivalent nonprojected values are easy to obtain.

In the case of reduced [2Fe−2S] clusters, the Heisenberg exchange coupling constant $J_{\text{Heis}}(\text{rd})$ cannot be directly computed from the DFT difference $E^{\text{HS}}(\text{rd}) - E^{\text{BS}}(\text{rd})$ because of the interplay of the antagonistic delocalization (i.e., double-exchange B) and localization (i.e., trapping ΔE) terms. In Scheme 2, we represent the two localized configurations "a" and "b" on the left. The two corresponding Heisenberg spin ladders are separated by $2\Delta E$ (irrespective of spin). On the right, the action of an increasing $B(S + {}^1/_2)$ term is represented for each spin state. For $\Delta E = 0$ (i.e., when configurations "a" and "b" are degenerate), one recovers the double-exchange-only splitting $\pm B(S + {}^1/_2)$.

Therefore (see Scheme 2 or eq 2 with a constant offset),

Scheme 1

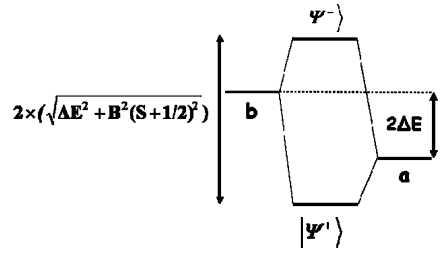

Scheme 2

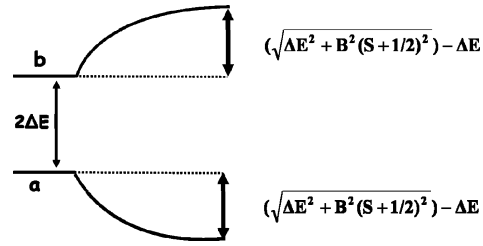

(64) Slater, J. C. *Phys. Rev.* **1951**, *81*, 385.
(65) Noodleman, L.; Case, D. A.; Aizman, A. *J. Am. Chem. Soc.* **1988**, *110*, 1001.
(66) Norman, J. G.; Ryan, P. B. J.; Noodleman, L. *J. Am. Chem. Soc.* **1980**, *102*, 4279.
(67) Ruiz, E.; Alvarez, S.; Cano, J.; Polo, V. *J. Chem. Phys.* **2005**, *123*, 164110.
(68) Ruiz, E.; Cano, J.; Alvarez, S.; Alemany, P. *J. Comput. Chem.* **1999**, *20*, 1391.

the energy of a given spin state S can be written as

$$\varepsilon_S(-) = \left(\frac{J_{\text{Heis}}}{2}\right)S(S+1) + \Delta E - \sqrt{\Delta E^2 + B^2(S+{}^1/_2)^2} \qquad (7a)$$

The DFT energy of the (partially delocalized) HS state must first be corrected in order to obtain the energy of the lowest (Heisenberg) localized $S = {}^9/_2$ state (the "a" configuration, $[Fe^{3+}-Fe^{2+}]$) needed for the computation of $J_{\text{Heis}}(\text{rd})$:

$$E^{\text{HS}}_{\text{loc}}(\text{rd}) = E^{\text{HS}}(\text{rd}) + \sqrt{\Delta E^2 + 25B^2} - \Delta E \qquad (7b)$$

Equation 7b reaches the expected limits for both $\Delta E \rightarrow 0$ [i.e., $E^{\text{HS}}_{\text{loc}}(\text{rd}) = E^{\text{HS}}(\text{rd}) - 5B$] and $\Delta E/B \gg 1$ [i.e., $E^{\text{HS}}_{\text{loc}}(\text{rd}) = E^{\text{HS}}(\text{rd})$]. We then compute $J_{\text{Heis}}(\text{rd})$ by applying the equation $J_{\text{Heis}}(\text{rd}) = [E^{\text{HS}}_{\text{loc}}(\text{rd}) - E^{\text{HS}}(\text{rd})]/(2S_AS_B)$ (which is analogous to eq 6) to the localized reduced state, for which $2S_AS_B = 10$. What is measured experimentally, usually by temperature-dependent experiments (magnetic susceptibility, NMR, relaxation, Mössbauer quadrupole splittings, etc.) is the energy difference between the $S = {}^3/_2$ and $S = {}^1/_2$ spin states, which is equal to ${}^3/_2J_{\text{eff}}(\text{rd})$, where $J_{\text{eff}}(\text{rd})$ is the effective exchange coupling constant, given by

$$J_{\text{eff}}(\text{rd}) = J_{\text{Heis}}(\text{rd}) - \frac{2}{3}\left(\sqrt{\Delta E^2 + 4B^2} - \sqrt{\Delta E^2 + B^2}\right) \qquad (8)$$

In addition to the Heisenberg term, there is an additional contribution, denoted as E_{Ferro}, which favors ferromagnetic alignment of the spins (since this is not a Heisenberg-type ferromagnetic coupling, it is not written as J_{Ferro}). In Figure S1 in the Supporting Information, the ratio (E_{Ferro}/B) is plotted as a function of $\Delta E/B$. For a given value of the double-exchange constant B, the magnitude of E_{Ferro} decreases for increasing ΔE values (i.e., increasing electronic localization), as expected.

g Tensors and g_{av} Values. We continue our phenomenological approach by computing total **g** tensors as linear combinations of fictitious local $\mathbf{g}_A$ and $\mathbf{g}_B$ tensors, thus assuming that the zero-field splitting terms are small compared to the exchange coupling constants.[69] In the case of full electronic delocalization, the corresponding **g** tensor can be written in a general way as

$$\mathbf{g}^{\text{deloc}} = \frac{1}{2}\left(\frac{5}{9}\mathbf{g}_A^{3+} + \frac{4}{9}\mathbf{g}_B^{2+}\right) + \frac{1}{2}\left(\frac{4}{9}\mathbf{g}_A^{2+} + \frac{5}{9}\mathbf{g}_B^{3+}\right) \qquad (9)$$

where $\{\mathbf{g}^{2+,3+}_{A,B}\}$ are local $\mathbf{g}_A$ and $\mathbf{g}_B$ tensors for monomers in the 2+ and 3+ oxidation states and the coefficients ${}^5/_9$ ($=S^{3+}/S$) and ${}^4/_9$ ($=S^{2+}/S$) result from spin-coupling algebra for parallel local spin alignment.[70] Because of the positive spin-projection coefficients, $g^{\text{deloc}}_{\text{av}} > g_e$ ($\approx$2.0023). The $\Delta\mathbf{g}$ tensors for the $S = {}^1/_2$ and $S = {}^9/_2$ states differ by a factor of 9, whereas the local $\mathbf{g}_A$ and $\mathbf{g}_B$ tensors are identical. However, eq 9 fails to account for the fact that the local iron formal charges change from 2+ or 3+ to 2.5+ upon delocalization. In practice, we extracted the local $\mathbf{g}_A$ and $\mathbf{g}_B$ tensors directly from the HS spin states converged using DFT methods. Numerically, for all of the systems considered, we found $g^{\text{deloc}}_{\text{av}}({}^1/_2) = 2.030 \pm 0.005$ (see Methodology).

In the case of full electronic localization (formally, $\Delta E/B \rightarrow \infty$), the local $\mathbf{g}_A$ and $\mathbf{g}_B$ tensors can be extracted from the localized BS states:

$$\begin{aligned} \mathbf{g}^{\text{loc}}_a &= \frac{7}{3}\mathbf{g}_A^{3+} - \frac{4}{3}\mathbf{g}_B^{2+} \qquad (c_a{}^2 = 1, c_b{}^2 = 0) \\ \mathbf{g}^{\text{loc}}_b &= -\frac{4}{3}\mathbf{g}_A^{2+} + \frac{7}{3}\mathbf{g}_B^{3+} \qquad (c_a{}^2 = 0, c_b{}^2 = 1) \end{aligned} \qquad (10)$$

Because of the terms containing −4/3, eq 10 indicates that *electronic localization will decrease the value of* g_{av} compared with the delocalized value of 2.03.

In order to derive the expression for g_{av} in the general (partially localized/delocalized) case, we need to properly weigh the two limits (localized and delocalized) as a function of the ratio $\Delta E/B$. We propose the following derivation, which relies on the fact that we are interested only in the isotropic g_{av} value for the **g** tensor rather than in the values of the three individual components $\{g_i\}$. It can then be shown that the 4×4 problem involving the four localized functions $\Psi_a(\pm{}^1/_2)$ and $\Psi_b(\pm{}^1/_2)$ (two Kramers doublets) is formally equivalent to introducing in eq 1 the (localized) Zeeman terms $Z^{\text{loc}}_a = \beta H g^{\text{loc}}_a$ and $Z^{\text{loc}}_b = \beta H g^{\text{loc}}_b$, where g^{loc}_a and g^{loc}_b are average **g**-tensor values; in other words, $E_a \rightarrow E_a + Z^{\text{loc}}_a$ and $E_b \rightarrow E_b + Z^{\text{loc}}_b$. Moreover, in order to recover the proper (delocalized) limit when $\Delta E/B \rightarrow 0$ (eq 9), we introduce the off-diagonal term $\delta Z = Z^{\text{deloc}} - Z^{\text{ref}}$, where $Z^{\text{deloc}} = \beta H g^{\text{deloc}}_{\text{av}}$ and $Z^{\text{ref}} = (Z^{\text{loc}}_a + Z^{\text{loc}}_b)/2$ (i.e., the average of the two diagonal terms), and replace $-E_B$ by $-E_B + \delta Z$ in eq 1. After solving the determinant, developing the solutions to first order in $Z/\Delta E$ and Z/B, and expressing them in terms of the **g** tensors, we finally obtain

$$g_{\text{av}} = \frac{g^{\text{loc}}_a + g^{\text{loc}}_b}{2} + \frac{\Delta E(g^{\text{loc}}_a - g^{\text{loc}}_b)}{2\sqrt{\Delta E^2 + B^2}} + \frac{B}{\sqrt{\Delta E^2 + B^2}}\left(g^{\text{deloc}} - \frac{g^{\text{loc}}_a + g^{\text{loc}}_b}{2}\right) \qquad (11)$$

Alternatively, upon use of eqs 3 and 5, eq 11 becomes

$$g_{\text{av}} = c_a{}^2 g^{\text{loc}}_a + c_b{}^2 g^{\text{loc}}_b + 2c_ac_b\left(g^{\text{deloc}} - \frac{g^{\text{loc}}_a + g^{\text{loc}}_b}{2}\right) \qquad (12)$$

For illustrative purposes, let us consider the case of the Rieske proteins, for which $g^{\text{loc}}_a \approx g^{\text{loc}}_b \approx 1.88$ and $g^{\text{deloc}} \approx 2.03$ (taken from Table 2 in the Results and Discussion). Substituting these values into eq 12 gives $g_{\text{av}} \approx 1.88 + 2c_ac_b(0.15)$. Figure 1 shows the variation of g_{av} as a function of $\Delta E/B$ within the corresponding delocalized (left) and localized (right) limits. The experimental g_{av} value of 1.91 is reached for $\Delta E/B \approx 5$. More generally, for each system we have computed the four local tensors $\{\mathbf{g}^{2+,3+}_{A,B}\}$ and plotted g_{av} as a function of the ratio $\Delta E/B$.

B. Explicit Vibronic Coupling and Static Asymmetries. In what follows, we will separately treat two types of contributions to the total valence trapping term ΔE:

(69) Schäfer, K.-O.; Bittl, R.; Zweygart, W.; Lendzian, F.; Haselhorst, G.; Weyhermüller, T.; Wieghardt, K.; Lubitz, W. *J. Am. Chem. Soc.* **1998**, *120*, 13104.

(70) Sinnecker, S.; Neese, F.; Noodleman, L.; Lubitz, W. *J. Am. Chem. Soc.* **2004**, *126*, 2613.

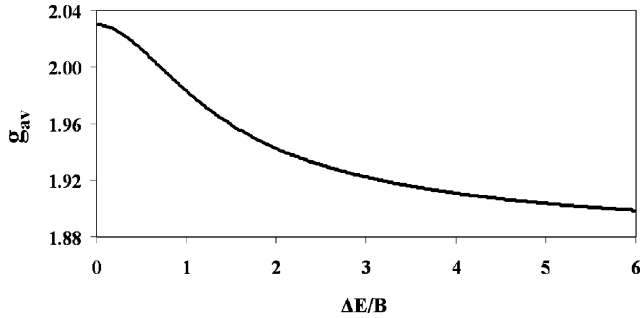

Figure 1. g_{av} as a function of the ratio $\Delta E/B$ for a simple Rieske model with $g^{loc} = 1.88$ and $g^{deloc} = 2.03$.

Table 2. Values of g_{av} for Plant-Type and Rieske Models

ligands					
Fe#1	Fe#2	g_a(BS1)	g_b(BS2)	ΔE(HS)/B	g_{av}
		Rieske Models[a]			
$(SCH_3)_2$	$(NH_3)_2$	1.873	1.853	4.88	1.887
$(SCH_3)_2$	$(Imid)_2$	1.873	1.881	5.59	1.908
$(SCH_3)_2$	$(His)_2$	1.873	1.871	4.34	1.906
$(Cys)_2$	$(NH_3)_2$	1.879	1.871	4.77	1.903
$(Cys)_2$	$(Imid)_2$	1.879	1.879	4.95	1.909
$(Cys)_2$	$(His)_2$	1.879	1.873	4.70	1.905
		Plant-Type Models[b]			
$(SCH_3)_2$	$(SCH_3)_2$	1.884	1.881	1.02	1.986
$(SCH_3)_2$	$(Cys)_2$	1.881	1.912	0.47	2.011
$(Cys)_2$	$(SCH_3)_2$	1.912	1.881	0.83	2.009
$(Cys)_2$	$(Cys)_2$	1.923	1.925	0.54	2.017

[a] Based on the 1JM1 PDB file. [b] Based on the 1CZP PDB file.

(1) the vibronic coupling that affects the iron−sulfur bridge and ligand relative distances (i.e., ΔE_{vib}) and (2) all of the other static terms (i.e., ΔE_{stat}). Among the static contributions, we first set aside the effect of chemical asymmetry (i.e., ΔE_{chem}), which prohibits the vibronic term from being treated with a common set of parameters for both iron sites. For [2Fe−2S] clusters having sulfur-based ligands (SCH_3 and cysteine), the static term includes the ligand orientation effect (i.e., ΔE_Ω), which is monitored through Fe−Fe−S−C dihedral angles $\{\Omega_i\}$, and, if needed, solvent contributions (i.e., ΔE_{solv}). We will then show how to semiquantitatively introduce the chemical asymmetry term ΔE_{chem}, first for Rieske centers (N vs S ligands), where the effect of this asymmetry is the strongest, and then for Fd's and Rieske mutants.

Let us examine the case of plant-type ferredoxins with chemical symmetry (i.e., four identical sulfur-based ligands, with $\Delta E_{chem} \approx 0$) for which one unique set of (k, λ) vibronic parameters is sufficient. In this case, the vibronic mechanism[26–29,71] involves electron–nuclear coupling λQ along the vibrational coordinate Q, defined as $2^{-1/2}(Q_A - Q_B)$, where Q_A and Q_B describe the breathing motions of the monomeric subunits A and B, respectively. The redox-induced difference in iron−ligand distances, Δr, is related to Q through the expression $\Delta r = Q/2^{1/2}$. These motions are monitored by the corresponding iron−sulfur (bridge and ligand) distances. The effect of the vibronic-coupling parameter λ is counteracted by a restoration force of the form $^1/_2 kQ^2$, where k is the force constant for nuclear distortion. Therefore, within the harmonic approximation, we have:

$$E_a = E_a(\text{stat}) + E_a(\text{vibronic}) = E_a(\text{stat}) + \frac{1}{2}kQ^2 + \frac{\lambda Q}{\sqrt{2}}$$
$$E_b = E_b(\text{stat}) + E_b(\text{vibronic}) = E_b(\text{stat}) + \frac{1}{2}kQ^2 - \frac{\lambda Q}{\sqrt{2}} \quad (13)$$

We wish to "build up" a plant-type Fd [2Fe−2S] cluster in three steps: (i) no double-exchange term ($B = 0$) and no active (ligand) trapping force ΔE_{stat}; (ii) B is nonzero while $\Delta E_{stat} \approx 0$; (iii) both B and ΔE_{stat} are operative. The first two cases can be solved analytically, whereas the third one must be approached from a numerical point of view.

Case (i): B = 0 and ΔE_{stat}= 0. For this fully localized (Robin and Day class I) system, eq 2 becomes

$$\varepsilon_S(\pm) = \left(\frac{J_{Heis}}{2}\right)S(S+1) + \frac{1}{2}kQ^2 \pm \frac{\lambda Q}{\sqrt{2}} \quad (14a)$$

to which application of the condition $\partial\varepsilon_S(\pm)/\partial Q = 0$ yields the following expression for the optimal coordinates $Q_{opt}(\pm)$:

$$Q_{opt}(\pm) = \pm\frac{\lambda}{k\sqrt{2}} \quad (14b)$$

Equation 14b shows that the optimal coordinates Q_{opt} are independent of the spin S. The energy of the intervalence (metal-to-metal) band, λ^2/k, is given by the difference in the energies of the (+) and (−) curves at $Q_{opt}(-)$. A symmetrical stretching vibrational quantum, ν, varying from 250 to 450 cm^{-1} {on the basis of resonance Raman data measured for rubredoxin, desulforedoxin, and the [Fe(S_2-*o*-xyl)$_2$] model complex} yields a range of $1200 \le \lambda^2/2k \le 3860$ cm^{-1} (see ref 72 and references therein). For example, in the explicit case of the [Fe(S_2-*o*-xyl)$_2$] model complex, $\Delta r = 0.089$ Å, where Δr is the redox-induced (2+/3+) difference in metal−sulfur (bridge/ligand) bond lengths for monomers. With two strong resonance Raman bands at 297 and 321 cm^{-1} for the oxidized complex, we have $k \approx$ 84 000–98 000 cm^{-1} and $\lambda^2/2k \approx$ 1330–1560 cm^{-1}. Gamelin et al.[73] proposed an alternative value of $\lambda^2/2k = 1830$ cm^{-1} (derived from the $\nu \approx 310$ cm^{-1} value measured for reduced [2Fe−2S] Fd's), resulting in a value of $k \approx 91\,500$ cm^{-1}. All of these experimental data yield the average values $k \approx$ 91 000 cm^{-1} and $\Delta E_{vib} = \lambda^2/2k \approx 1600$ cm^{-1}.

This last estimate of ΔE_{vib} depends on $\Delta r = Q/2^{1/2}$ (since $\lambda \approx 2k\Delta r$, it follows that $\lambda^2/2k \approx 2k\Delta r^2$). From a computational point of view, we first consider the simple [$Fe^{n+}(SH)_4$] ($n = 2, 3$) model with geometry optimization of both redox states at the VBP level (see Methodology). From the difference in the energies of the oxidized and reduced optimized geometries ($\Delta r = 0.085$ Å) converged in the reduced state [E_{rd}(ox) − E_{rd}(rd) = 970 cm^{-1}], we have $k \approx 970/(0.085)^2 \approx 134\,250$ cm^{-1} (in the harmonic approximation) and the derived quantity $\lambda^2/2k = 1940$ cm^{-1}, in fair agreement with the above values.

It is the usual procedure to transfer to dimers the parameters derived from monomers, and it is assumed that

(71) Piepho, S. B. *J. Am. Chem. Soc.* **1990**, *112*, 4197.
(72) Borshch, S. A.; Bominaar, E. L.; Blondin, G.; Girerd, J.-J. *J. Am. Chem. Soc.* **1993**, *115*, 5155.
(73) Gamelin, D. R.; Bominaar, E. L.; Kirk, M. L.; Wieghardt, K.; Solomon, E. I. *J. Am. Chem. Soc.* **1996**, *118*, 8085.

the bridge and ligand atoms on the reduced iron site in the [2Fe−2S] dimer behave the same as the four ligand atoms in the monomer upon reduction (symmetric breathing mode). In the appendix in the Supporting Information, we show that this is not exactly the case for the [2Fe−2S] BS states presented as a superposition of monomer states (in contrast to recent ab initio Möller–Plesset-optimized geometries of [2Fe−2S] clusters[74]).

In case (ii) below, we attempt to estimate the value of $\Delta E_{vib} = \lambda^2/2k$ upon introduction of the double-exchange B term. We also need the quantity $\Delta r_{vib} = Q_{opt}(-)/2^{1/2} = \lambda/2k$ (the optimal value in the absence of double-exchange), defined through $\Delta E_{vib} = \lambda \Delta r_{vib} = 2k\Delta r_{vib}^2$.

Case (ii): $B \neq 0$ and $\Delta E_{stat} \approx 0$. Upon inclusion of the double-exchange term ($B \neq 0$), we now have:[26,29]

$$\varepsilon_S(\pm) = \left(\frac{J_{Heis}}{2}\right)S(S+1) + \frac{1}{2}kQ^2 \pm \sqrt{\left(\frac{\lambda Q}{\sqrt{2}}\right)^2 + B^2(S+{}^1/_2)^2} \quad (15a)$$

For each spin S and for B values satisfying the condition $\Delta E_{vib} \geq B(S + {}^1/_2)$, the vibronic coupling will be strong enough to result in an asymmetrical (Robin and Day class II) valence-trapped [2Fe−2S] cluster; applying the condition $\partial\varepsilon_S(-)/\partial Q = 0$ yields

$$\frac{\lambda Q_B(-)}{\sqrt{2}} = \lambda \Delta r_B(S) = \sqrt{\Delta E_{vib}{}^2 - B^2(S+{}^1/_2)^2} \quad (15b)$$

Let us define the effective vibronic coupling as $\Delta E_{vib}^{eff}(S) = \lambda \Delta r_B(S) = \Delta E_{vib}[\Delta r_B(S)/\Delta r_{vib}]$. In Figure S2 in the Supporting Information, we have plotted $\Delta E_{vib}^{eff}(S)/\Delta E_{vib} = \Delta r_B(S)/\Delta r_{vib}$ as a function of ΔE_{vib} for $S = {}^1/_2$ and ${}^3/_2$.

In contrast, when $\Delta E_{vib} \leq B(S + {}^1/_2)$, the double-exchange term dominates (Robin and Day class III), and $Q_B(-) = 0$ (i.e., $\Delta r_B = 0$). It is possible to link the value of the ratio $\Delta E_{vib}/B$ to structural data, with $\Delta r_B = Q_B/2^{1/2}$ (where $0 \leq \Delta r_B < \Delta r_{vib}$ necessarily). From eq 15b, it can be shown that under the condition $\Delta E_{vib} \geq B(S + {}^1/_2)$, the vibronic coupling is

$$\Delta E_{vib} = k\Delta r_B(S)^2 + \sqrt{B^2(S+{}^1/_2)^2 + k^2\Delta r_B(S)^4} \quad (15c)$$

In eq 15c, when $B = 0$, one recovers $\Delta E_{vib} = 2k\Delta r_{vib}^2$. Moreover, the larger B is, the smaller Δr_B becomes. Let us consider the [2Fe−2S] ferredoxin from the cyanobacterium *Anabaena* in its reduced state.[49] To obtain first an estimate of B, we constructed the [2Fe−2S](SCH$_3$)$_4$ model cluster derived directly from the 1CZP structure (without geometry optimization). From eqs 3−5, we found $B \approx 700$ cm^{-1} (see Table 3 in the Results and Discussion). If we assume that an average Δr_B value for the $S = {}^1/_2$ state can be obtained from the ligand and bridging Δr values (0.024 and 0.052 Å, respectively) and that $k \approx 100\,000$ cm^{-1}, from eq 15c we obtain $\Delta E_{vib} \approx 890 \pm 130$ cm^{-1}. In turn, $\Delta r_{vib} = (\Delta E_{vib}/2k) \approx 0.067$ Å, which is intermediate between the value computed for the [2Fe−2S](Cl$_4$) BS state (see the appendix in the Supporting Information) and those computed or measured for iron−sulfur monomers (0.085 Å). This estimate of ΔE_{vib} is approximately half the value found in monomers (1600 cm^{-1}).

Table 3. Exchange Coupling Constants Computed for Plant-Type, Putidaredoxin-Type, and Rieske [2Fe−2S] Clusters

	1CZP[a]		1XLQ[b]		1JM1[c]	
	VBP	B3LYP	VBP	B3LYP	VBP	B3LYP
J_{Heis}(ox)	772	481	829	527	783	443
exp (ox)	366		>460		360	
B	702	(628)	822	(758)	280	(89)
ΔE(HS)	720	(974)	1151	(994)	1400	(1596)
E_{Ferro}	−382		−39		−53	
E_{Ferro} (+ solvent)	176		202		nc[d]	
J_{Heis}(rd)	709	413	1025	695	761	457
J_{eff}	327	31	630	300	708	404
J_{eff} (+ solvent)[e]	503	207	832	502	708	> 404
exp (rd)	150–200		340, 540		130, 200, 380	

[a] Ferredoxin from *Anabaena* (PDB entry 1CZP), with SCH$_3$ ligands. [b] Putidaredoxin from *P. putida* (PDB entry 1XLQ). [c] Rieske protein II from *S. acidocaldarius* (PDB entry 1JM1), with SCH$_3$ and imidazole ligands. [d] Not computed. [e] Solvent offset: $\Delta E_{solv}/B = 2.0$.

At the optimal geometry, the energy $\varepsilon_S(-)$ (see Figure S3 in the Supporting Information) is given by

$\Delta E_{vib} < B(S + {}^1/_2)$:

$$\varepsilon_S(-) = \left(\frac{J_{Heis}}{2}\right)S(S+1) - \left(\frac{B^2}{2\Delta E_{vib}}\right)S(S+1) - \frac{\Delta E_{vib}}{2} - \frac{B^2}{8\Delta E_{vib}} \quad (15d)$$

$\Delta E_{vib} < B(S + {}^1/_2)$:

$$\varepsilon_s(-) = \left(\frac{J_{Heis}}{2}\right)S(S+1) - B(S+{}^1/_2)$$

where the term $J_{Ferro} = -B^2/\Delta E_{vib}$ serves as a Heisenberg-type ferromagnetic contribution, resulting in an effective exchange coupling constant $J_{eff} = J_{Heis} + J_{Ferro}$. Notice that eq 15d is an exact expression. In Figure S4 in the Supporting Information, we have plotted $J_{eff} = {}^2/_3(\varepsilon_{3/2} - \varepsilon_{1/2})$ as a function of ΔE_{vib}. It can be verified that in order to reach the experimental J_{eff} range of 150–200 cm^{-1} measured for plant-type Fd's,[58,61,62] ΔE_{vib} must have a value in the range 2000−3000 cm^{-1}. We will see below that taking static contributions into account decreases the value of ΔE_{vib}.

In order to estimate $\Delta E_{vib}^{eff}({}^1/_2)$ from the vegetative *Anabaena* [2Fe−2S] cluster,[49] we removed the static contribution ΔE_{stat} (i.e., the ligand conformation effects) to the [2Fe−2S](SCH$_3$)$_4$ model mentioned above by setting the four Fe−Fe−S−C dihedral angles to 0° (while strictly preserving all of the other structural parameters). From the HS state (eqs 3−5), we found $\Delta E/B \approx 0.55$. As this value reflects only the degree of structural (vibronic) asymmetry of the [2Fe−2S] core, it can be equated with $\Delta E_{vib}^{eff}/B$. From eq 15b with $B \approx 700$ cm^{-1}, we obtain $\Delta E_{vib} \approx 800$ cm^{-1}, in fair agreement with the value derived above (890 cm^{-1}). This small value of ΔE_{vib} is barely large enough to localize the reducing electron on one iron site. The key to the experi-

mentally observed partial electronic localization is found in the additional static contributions.

There is an alternative, more approximate expression of $\varepsilon_S(-)$ that will suit our purposes when we consider electronically localized systems (i.e., Rieske centers). For $t_B(S) = \Delta r_B(S)/\Delta r_{vib} < 1$, combining eqs 15a and 15d (applying a constant offset of $\Delta E_{vib}/2$ to 15a) gives

$$\varepsilon_S(-) = \left(\frac{J_{Heis}}{2}\right)S(S+1) + \left(\frac{\Delta E_{vib}}{2}\right)[1 + t_B(S)^2] - \sqrt{\Delta E_{vib}{}^2 t_B(S)^2 + B^2(S+{}^1\!/_2)^2} \quad (15e)$$

For a large value of the ratio $\Delta E_{vib}/B(S + {}^1\!/_2)$, $t_B(S) \rightarrow 1$ and eq 15e becomes equivalent to the phenomenological expression 7a with $\Delta E = \Delta E_{vib}$. In Figure S4 in the Supporting Information, we have also plotted $J_{eff} = {}^2\!/_3(\varepsilon_{3/2} - \varepsilon_{1/2})$ computed using eq 7a as a function of ΔE_{vib}. This figure shows that the exact (eqs 15a,d,e) and approximate (eq 7a) curves converge only for large values of ΔE_{vib}.

Case (iii): $B \neq 0$ and $\Delta E_{stat} \neq 0$. For this general case, eq 2 becomes[24,2626,29]

$$\varepsilon_S(\pm) = \left(\frac{J_{Heis}}{2}\right)S(S+1) + \frac{1}{2}kQ^2 \pm \sqrt{\left(\Delta E_{stat} + \frac{\lambda Q}{\sqrt{2}}\right)^2 + B^2(S+{}^1\!/_2)^2} \quad (16a)$$

The search for an analytical expression for $\Delta r(S) = Q_{opt}/2^{1/2}$ (where $\Delta r_B \leq \Delta r \leq \Delta r_{vib}$) turns out to be cumbersome (see, however, ref 75). In the absence of double-exchange ($B = 0$), there are two minima [at $\pm\lambda/(2^{1/2}k)$] when $\Delta E_{stat} < \Delta E_{vib}$ but only one minimum [at $+\lambda/(2^{1/2}k)$] when $\Delta E_{stat} > \Delta E_{vib}$. Upon inclusion of $B \neq 0$, we expect $\partial\varepsilon(-)/\partial Q = 0$ to yield two roots for very small ΔE_{stat} values. For larger ΔE_{stat} values, only one root (with $\Delta r > 0$) should be found.

Here we focus on that positive root and search numerically for values of (ΔE_{stat}, Δr) pairs that satisfy $\partial\varepsilon(-)/\partial Q = 0$, i.e., pairs for which

$$\Delta E_{stat} + \Delta E_{vib}\left(\frac{\Delta r(S)}{\Delta r_{vib}}\right) = B(S+{}^1\!/_2)\frac{\Delta r(S)}{\sqrt{\Delta r_{vib}{}^2 - \Delta r(S)^2}} \quad (16b)$$

Figure 2 shows $\Delta r(S)$ as a function of ΔE_{stat} for all of the spin states $S = {}^1\!/_2, {}^3\!/_2, \ldots, {}^9\!/_2$, for $\Delta E_{vib} = 800$ cm^{-1} (i.e., $\Delta r_{vib} = 0.067$ Å) and $B = 700$ cm^{-1}. As soon as ΔE_{stat} becomes nonzero, all of the spin states start to localize on one iron site. This contrasts with the case where only vibronic coupling is at work, in which only the $S = {}^1\!/_2$ and possibly the $S = {}^3\!/_2$ states are partially localized.

In close analogy to eq 15e, use of eq 16b allows eq 16a to be rewritten as

$$\varepsilon_S(-) = \left(\frac{J_{Heis}}{2}\right)S(S+1) + \left(\frac{\Delta E_{vib}}{2}t(S)^2 + \frac{\Delta E_{vib}}{2} + \Delta E_{stat}\right) - \sqrt{[\Delta E_{vib}t(S) + \Delta E_{stat}]^2 + B^2(S+{}^1\!/_2)^2} \quad (16c)$$

where $t(S) = \Delta r(S)/\Delta r_{vib}$. Inside the square root, the vibronic contribution appears as an effective term $\Delta E_{vib}^{eff} = \Delta E_{vib}t(S)$ (see Figure S5 in the Supporting Information). It can be numerically verified (see Figure S6 in the Supporting Information) that for ΔE_{stat} larger than ~1000 cm^{-1}, use of eqs 16a and 16c again becomes practically indistinguishable from eq 7a, this time with $\Delta E = \Delta E_{vib} + \Delta E_{stat}$. The larger the nonvibronic trapping forces (ΔE_{stat} in this case) are, the closer the effective vibronic contribution comes to its maximum value ΔE_{vib}. We will specifically deal with the contribution to ΔE_{stat} from the ligand orientation (i.e., ΔE_Ω) in plant-type Fds in the Results and Discussion. Replacing the sulfur ligands with nitrogen-based (i.e., NH_3, imidazole, or histidine) or oxygen-based (i.e., OH^-, $OSCH_3$, or serine) ligands creates a chemical asymmetry between the two iron sites, inducing a priori a large offset ΔE_{chem} that may dominate over the double-exchange and vibronic terms.

A proper analytical treatment of Rieske centers and Fd/Rieske mutants requires a reformulation of the whole static and dynamic problem, using various k and λ coefficients reflecting the ligand (S/N/O) combinations on the two iron sites. We have chosen not to go in that direction. Instead, for these systems, we have adopted a more phenomenological approach that involves computing ΔE in each case and then relying on eq 7a, where our ansatz is to equate ΔE with $\Delta E_{chem} + \Delta E_{vib} + \Delta E_\Omega + \Delta E_{solv} + \cdots$ (depending on the complexity of the DFT models, their geometries, etc.).

In order to compare the approximate expression (eq 7a) with the exact one (eqs 16a and 16c), in Figure 3 we have plotted J_{eff} as a function of ΔE_{stat} (with $\Delta E_{vib} = 800$ cm^{-1}). It can be seen that the exact (continuous line) and approximate (upper dotted line, with a vibronic offset of 800 cm^{-1}) curves become numerically equivalent for values of ΔE_{stat} larger than 1000 cm^{-1}. For plant-type ferredoxins, experimental J_{eff} values of 150–200 cm^{-1} have been measured; from Figure 3, this would require that $1000 \leq \Delta E_{stat} \leq 1500$ cm^{-1} (i.e., $1.4 \leq \Delta E_{stat}/B \leq 2.1$). We will see below the importance of solvation effects in reaching this range in some cases. On the other hand, in the case of XO clusters

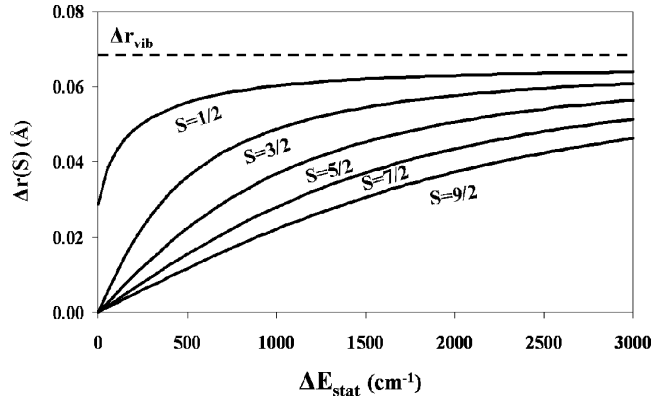

Figure 2. $\Delta r(S)$ as a function of ΔE_{stat} for spin states $S = {}^1\!/_2$ to ${}^9\!/_2$, with $B = 700$ cm^{-1} and $\Delta E_{vib} = 800$ cm^{-1} ($\Delta r_{vib} = 0.067$ Å).

(74) Higashi, M.; Kato, S. *J. Phys. Chem. A* **2005**, *109*, 9867.
(75) Borras-Almenar, J. J.; Corronado, E.; Ostrovsky, S. M.; Palii, A. V.; Tsukerblat, B. S. *Chem. Phys.* **1999**, *240*, 149.

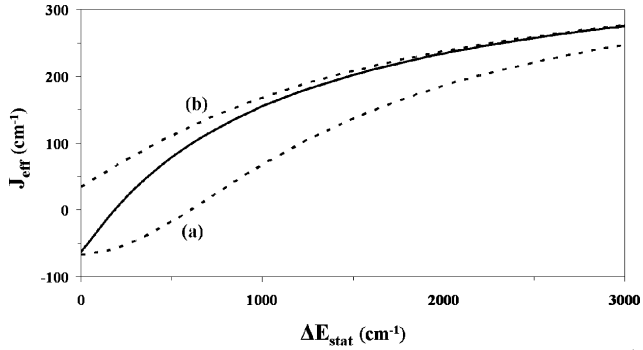

Figure 3. J_{eff} as a function of ΔE_{stat}: (continuous line) computed using eqs 16a and 16c, with $\Delta E_{vib} = 800$ cm^{-1}, $J_{Heis} = 400$ cm^{-1}, and $B = 700$ cm^{-1}; (dotted lines) computed using eq 7a with minimum and maximum vibronic offsets of (a) 0 and (b) 800 cm^{-1}, respectively.

II, the possibility of getting small J_{eff} values through small ΔE_{stat} values ($J_{eff} \approx 50$ cm^{-1} for $\Delta E_{stat} \approx 300$ cm^{-1}) becomes very interesting.

In the case of Rieske centers and possibly Fd/Rieske mutants, we do not have exact analytical or numerical expressions for either the spin-state energies or, therefore, the exchange coupling constants. For these cases, we have used eq 7a, as ΔE_{stat} (because of the ΔE_{chem} offset) is expected to be large enough (see Table 2 in the Results and Discussion).

Methodology

Calculation of *g* Tensors. The components of the local **g**(Fe) tensors for [Fe(S-ligand)$_4$] high-spin monomers can be computed to second order according to the following general expression:[48]

$$g(\mathrm{Fe})_{ij} \approx g_e\delta_{ij} - \frac{2\xi_{Fe}}{2S_{Fe}}\left(\sum_{maj} - \sum_{min}\right)\sum_{n=1}^{N}\frac{\langle 0|L_i|n\rangle\langle n|L_j|0\rangle}{E_n - E_0} \qquad (17)$$

where ξ_{Fe} is the iron one-electron spin–orbit constant (400 cm^{-1} for Fe^{2+}, having spin $S_{Fe} = 2$, and 460 cm^{-1} for Fe^{3+}, having spin $S_{Fe} = {}^5/_2$), "maj" and "min" stand for the majority and minority spin MOs, respectively, and E_0 and E_n are the MO energies of the ground and excited states, respectively.

For the d^5 ferric ion, the deviation of g_{ii} from g_e originates from a sum of minor ligand-to-metal contributions and usually has values in the range $0.01 \le \Delta g(Fe^{3+})_{ii} \le 0.03$ (with $\Delta g_{ii} \equiv g_{ii} - g_e$). In this work, we have used the value $\Delta g_{iso}(Fe^{3+}) = 0.02$. The equivalent isotropic contribution for the ferrous ions, $\Delta g_{iso}(Fe^{2+})$, was also set equal to 0.02. In addition to this isotropic term, the sixth (minority-spin) electron of the d^6 high-spin configuration is the main source of the anisotropy in the local $\mathbf{g}(Fe^{2+})$ tensor. As a consequence, for a ferrous ion, eq 17 becomes

$$g(\mathrm{Fe}^{2+})_{ij} \approx (g_e + \Delta g_{iso})\delta_{ij} + \frac{2\xi_{Fe}}{2S_{Fe}}\sum_{min}\sum_{n=1}^{N}\frac{\langle 0|L_i|n\rangle\langle n|L_j|0\rangle}{E_n - E_0} \qquad (18)$$

Local **g** tensors for Fe^{2+} and Fe^{3+} monomers can be computed for BS states of reduced [2Fe−2S] dimers. The BS state[76] is not a pure spin state (here, $S = {}^1/_2$); instead, it is a single-determinant Kohn–Sham wave function of mixed spin (with $M_S = {}^1/_2$) and spatial broken symmetries, where the α and β electrons are spatially localized on the left and right metal sites, respectively.[76–78] The wave function can be written as $\Psi_{BS}(M_S = {}^1/_2) = \sum_S C_S\Psi_S(M_S = {}^1/_2)$, where $\{C_S\}$ are the appropriate Clebsch−Gordan coefficients and S runs from ${}^1/_2$ to ${}^9/_2$. This artificial spatial localization is the key computational feature allowing for the computation of local **g** tensors. BS states are, by construction, electronically localized (i.e., formally equivalent to the limit $\Delta E/B \to \infty$). In other words, BS states are very suitable for describing transition-metal dimers that "naturally" exhibit valence localization, such as Rieske type clusters. This is not the case, however, for chemically and geometrically symmetric clusters. This is a point whose implications and consequences have not been fully explored to date, although it weighs heavily on our method of computing both g_{av} values and exchange coupling constants J_{eff}.

In contrast, in our DFT computations, we always found $g^{HS} = 2.03 \pm 0.005$ for all of the systems. In the case of the $S = {}^9/_2$ state of the [2Fe−2S] cluster from *C. pasteurianum*, the g^{HS} value has been measured as 2.03–2.04.[15,23] As a consequence, we have used $g^{HS} = 2.03$ throughout this work.

DFT Calculations. All of the DFT calculations of the present study were performed using the Amsterdam Density Functional programs (ADF2006.01) developed by Baerends and co-workers.[79–84] Unless mentioned otherwise, we used the VBP exchange-correlation (XC) potential (Vosko, Wilk, and Nusair's exchange and correlation energy[85,86] completed by Becke's nonlocal gradient corrections to the exchange energy[87] as well as those of Perdew to the correlation energy;[88] both corrections are included in the self-consistent procedure). Alternatively, we also performed some calculations using hybrid exchange potentials, especially B3LYP,[89–91] mixing in 20% (the ADF default value) of the Hartree–Fock exchange into the XC potential. Finally, we used triple-ζ plus polarization basis sets for all of the atoms (Fe, S, O, N, C, and H). For all of the cluster models, we verified that with ADF2006, only the first d−d gap (either metal → metal or metal → ligand) was accessible through the Slater transition procedure for the B3LYP hybrid potential, whereas all of the gaps can usually be computed when using standard (i.e., nonhybrid) XC potentials (such as VBP).

For the reasons listed in Appendix A, we decided to pursue our goal of rationalizing the distribution of the g_{av} values among various [2Fe−2S] (complex and protein) systems by converging the corresponding electronic structures using the VBP XC potential.

The **g** tensors and corresponding g_{av} values computed from BS states were obtained after scaling down the VBP (Slater) d−d transitions by a factor of 2. We computed the Heisenberg coupling constants J_{Heis} using both the VBP and B3LYP XC potentials (Tables S1 and S2 in the Supporting Information, respectively). Only the latter potential provided us with values comparable to experiment. However, the same B3LYP potential tended to exaggerate the values of the $\Delta E/B$ ratios with respect to the VBP results, as the magnetic orbitals in the HS state turned out to be more

(76) Noodleman, L. *J. Chem. Phys.* **1981**, *74*, 5737.
(77) Noodleman, L.; Davidson, E. R. *Chem. Phys.* **1986**, *109*, 131.
(78) Noodleman, L.; Norman, J. G. *J. Chem. Phys.* **1979**, *70*, 4903.
(79) Baerends, E. J.; Ellis, D. E.; Ros, P. *Chem. Phys.* **1973**, *2*, 41.
(80) Baerends, E. J.; Ros, P. *Chem. Phys.* **1973**, *2*, 52.
(81) Baerends, E. J.; Ros, P. *Int. J. Quantum Chem., Quantum Chem. Symp.* **1978**, *12*, 169.
(82) Bickelhaupt, F. M.; Baerends, E. J.; Ravenek, W. *Inorg. Chem.* **1990**, *29*, 350.
(83) teVelde, G.; Baerends, E. J. *J. Comput. Phys.* **1992**, *99*, 84.
(84) Ziegler, T. *Chem. Rev.* **1991**, *91*, 651.
(85) Painter, G. S. *J. Phys. Chem.* **1986**, *90*, 5530.
(86) Vosko, S. J.; Wilk, L.; Nusair, M. *Can. J. Phys.* **1980**, *58*, 1200.
(87) Becke, A. D. *Phys. Rev. A* **1988**, *38*, 3098.
(88) Perdew, J. P.; Wang, Y. *Phys. Rev. B* **1986**, *33*, 8800.
(89) Watson, M. A.; Handy, N. C.; Cohen, A. J. *J. Chem. Phys.* **2003**, *119*, 6475.
(90) Lee, C.; Yang, W.; Parr, R. G. *Phys. Rev. B* **1988**, *37*, 785.
(91) Becke, A. D. *J. Chem. Phys.* **1993**, *98*, 1372.

contracted. Therefore, J_{Heis} constants reported here were computed at the B3LYP level (including the correction depicted in Scheme 2 for HS states). The reported values of $\Delta E/B$ ratios for low-spin states were computed at the VBP level.

Geometries. Whenever feasible, we relied on protein crystallographic data. Our working model for the plant-type [2Fe−2S] Fds was based on the structure of the reduced *Anabaena* ferredoxin (PDB entry 1CZP), which was determined at atomic resolution (1.17 Å).[49] We considered the following ligands (while preserving the Fe−Fe−S−X dihedral angles): SH^-, SCH_3^- (SMe), and $SCH_2CH(NH_2)CO_2H^-$ [Cys (cysteine including the carbonyl group)]. We also considered the C49S mutant of the *Anabaena* ferredoxin (PDB entry 1QOA; resolution 1.70 Å)[8] in order to quantify the effect of ligand substitution on g_{av} and J_{eff}. In addition, we considered the crystallographic structure of reduced putidaredoxin from *Pseudomonas putida* (PDB entry 1XLQ; resolution 1.48 Å).[51] In the thioredoxin-like [2Fe−2S] family, we constructed models based on the WT ferredoxin from *A. aeolicus* (PDB entry 1M2A; resolution 1.50 Å), as well as the C55S (PDB entry 1M2B; resolution 1.25 Å) and C59S (PDB entry 1M2D; resolution 1.05 Å) mutants.[52]

All of our Rieske models were based on the crystal structure of the soluble domain of the reduced Rieske protein II (soxF) from *Sulfolobus acidocaldarius* (PDB entry 1JM1; resolution 1.11 Å).[92] The ligands used at the ferrous site in our models were NH_3, imidazole, and histidine [protonated ($N_2C_3H_4$) and deprotonated ($N_2C_3H_3^-$)]. At the ferric site, we used the ligands SH^-, SMe, and Cys.

We constructed various models representative of the XO family on the basis of available crystallographic data. Our basic model for both clusters I and II originated from the structure refinement of the aldehyde oxidoreductase from *Desulfovibrio gigas* (PDB entry 1VLB; resolution 1.28 Å).[93] We considered additional clusters I and II models based on the xanthine dehydrogenase isolated from bovine milk (PDB entry 1FO4; resolution 2.10 Å).[94]

Results and Discussion

A. Plant-type Ferredoxins versus Rieske-type Proteins. Effect of the Ligand Carbonyl Group on g_{av}. In this section, the **g** tensors were first computed for BS states, that is, we imposed full electronic localization. We constructed various plant-type Fd's [2Fe−2S](SR)$_4$ and Rieske models [2Fe−2S](NR′)$_2$(SR)$_2$ (SR = SCH_3^-, Cys; NR′ = NH_3, imidazole, histidine), starting from the 1CZP and 1JM1 PDB files, respectively. We searched for a ligand effect affecting the local ferrous **g**(Fe^{2+}) tensor.

For all of the Rieske models, the average **g** tensor value g_{av} turned out to be almost independent of the nature of the nitrogen-based ligands on the ferrous side: $g_{av} \approx 1.91$, except for the ligand combination $(NH_3)_2(SCH_3)_2$, where $g_{av} = 1.89$ (see Table 2). In contrast, for Fd's there was a significant increase in g_{av} (0.03 at this level of approximation) when the ferrous side (Fe#1) bore sulfur ligands with carbonyl (C═O) groups (i.e., Cys) as opposed to SMe groups.

The interplay between Fe d and carbonyl orbitals in the case of plant-type ferredoxins ($g_{av} = 1.96$) had already been hinted at in a previous DFT study of the process of electron transfer to fd-$NADP^+$ reductase (FNR) mediated by a [2Fe−2S] ferredoxin.[95] This may explain the fact that the g_1 values were quite dispersed. When trying to extract a gap value Δ_{xy} from the plot of $g_1 = g_z \approx \sin^2\theta/\Delta_{xy}$, Bertrand et al.[47] found Δ_{xy} values in the range 500–2000 cm^{-1}. As g_1 corresponds to the smallest of the d−d transitions, if the Fe d and C═O orbitals are quasi-degenerate, small structural variations around the ferrous ion may induce large variations among the g_1 values and smaller ones in g_2 and g_3. In contrast,[46] for the case of the Rieske proteins and related models, where there is no quasi-degeneracy between the Fe d and histidine carbonyl orbitals, the g_1 values were nicely aligned when plotted as a function of $g_2 - g_3$, with very little dispersion of the values.

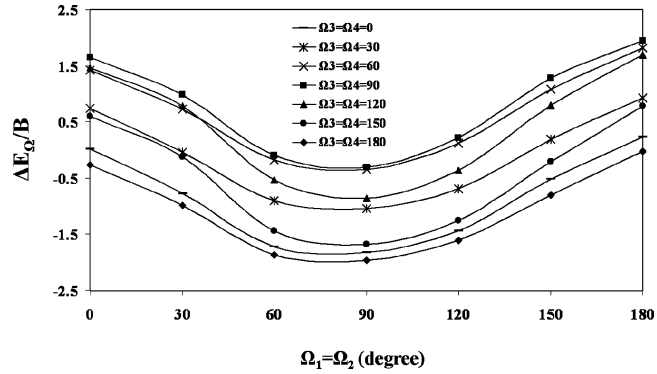

Figure 4. $\Delta E_\Omega/B$ as a function of $\Omega_1 = \Omega_2$ for various $\Omega_3 = \Omega_4$ values.

Ligand Orientation. In order to quantify the trapping effect ΔE_Ω due to the ligand orientations (which are characterized by their Fe−Fe−S−C dihedral angles $\{\Omega_i\}$), we turned to the [2Fe−2S](SCH$_3$)$_4$ model cluster derived from the original 1CZP structure ($\Omega_1 = \Omega_2 = 130°$, $\Omega_3 = 78°$, and $\Omega_4 = -123°$). We computed ΔE(HS)/B obtained from HS calculations (eq 4) after rotating the methyl group around the Fe−S bonds without additional geometry optimization [but keeping $\Omega_1 = \Omega_2$ on the ferrous site (Fe#1) and $\Omega_3 = \Omega_4$ on the ferric site (Fe#2), i.e., keeping an approximate C_2 symmetry, for the sake of simplicity]. At this level, we expected to have $\Delta E(\mathrm{HS}) \approx \Delta E_{vib}^{eff} + \Delta E_\Omega$ (see eq 16c inside the square root).

For the two C_{2v} configurations ($\Omega_{1,2} = \Omega_{3,4} = 0°$ or 180°), for which we expect ΔE_Ω to cancel for symmetry reasons, we found the same value of the ΔE(HS)/B ratio, 0.55, that was identified above [see Theory, Part B, Case (ii)] as the effective vibronic contribution $\Delta E_{vib}^{eff}/B = \Delta E_{vib}(\Delta r/\Delta r_{BS})$. The ratio $\Delta E_\Omega/B$ after subtraction of $\Delta E_{vib}^{eff}/B \approx 0.55$ from all of the ΔE(HS)/B values is shown in Figure 4 as a function of $\Omega_1 = \Omega_2$ (30° step) for various $\Omega_3 = \Omega_4$ values (30° step). Each plot was fitted separately by a function of the form $A\cos^2\Omega_{1,2} + B$ (the values of A and B are given in eqs S1 in the Supporting Information). We observe two things:

(i) For all of the plots, the magnitude of the (ligand) static term ΔE_Ω was far from negligible (with a maximum value

(92) Bönish, H.; Schmidt, C. L.; Shäfer, G.; Ladenstein, R. *J. Mol. Biol.* **2002**, *319*, 791.
(93) Rebelo, J. M.; Dias, J. M.; Huber, R.; Moura, J. J. G.; Romão, M. J. *J. Biol. Inorg. Chem.* **2001**, *6*, 791.
(94) Enroth, C.; Eger, B. T.; Okamoto, K.; Nishino, T.; Nishino, T.; Pai, E. F. *Proc. Natl. Acad. Sci. U.S.A.* **2000**, *97*, 10723.
(95) Morales, R.; Frey, M.; Mouesca, J.-M. *J. Am. Chem. Soc.* **2002**, *124*, 6714.

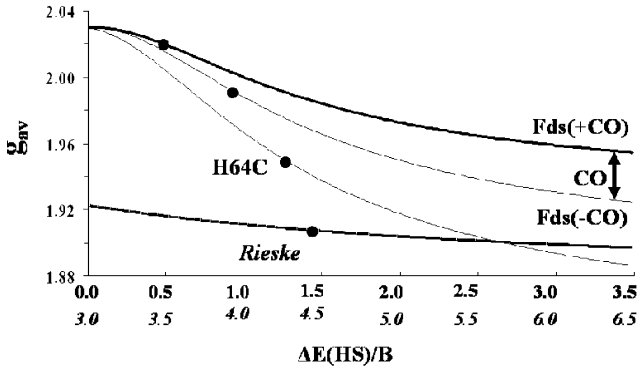

Figure 5. g_{av} as a function of the ratio $\Delta E/B$ for Fd and Fd mutant (upper x-axis scale) and Rieske [lower (italic) x-axis scale] systems. The Rieske curve is shifted by three $\Delta E/B$ units compared with the Fd curves.

of 2.0). Therefore, since each protein and model [2Fe−2S] complex is characterized by a specific set of angles $\{\Omega_i\}$, the ratio $\Delta E_\Omega/B$ is unique, requiring each case to be treated separately.

(ii) For some ligand conformations, the $\Delta E_\Omega/B$ ratio was negative, indicating that the reducing electron had jumped from Fe#1 (the naturally reduced iron site for plant-type Fd's) to Fe#2. This becomes important when comparing electronic delocalization in plant- and thioredoxin-type clusters.

We derived an approximate expression for $\Delta E_\Omega/B$ in Figure 4:

$$\frac{\Delta E_\Omega}{B} \approx -0.32\cos^2\Omega_{1,2}\cos^2\Omega_{3,4} + 2.29\cos^2\Omega_{1,2} - 1.54\cos^2\Omega_{3,4} - 0.43 \quad (19)$$

For the original 1CZP structure, $\Delta E(\mathrm{HS})/B \approx 1.03$, that is, $\Delta E_\Omega/B \approx 0.48$ or $\Delta E_\Omega \approx 340\ \mathrm{cm}^{-1}$. For that last value, with $\Delta E_{vib} \approx 800\ \mathrm{cm}^{-1}$, eq 15b is satisfied when $\Delta r \approx 0.053$ Å. This average Δr value can be compared to those measured for the original 1CZP structure: $\Delta r(\mathrm{ligand}) \approx 0.022$ Å and $\Delta r(\mathrm{bridge}) \approx 0.054$ Å.[49] The value we found (0.053 Å) represents a compromise achieved in the absence of additional exterior trapping forces (typically the solvent) and therefore stands as an upper limit.

In Figure 5, we have plotted the value of g_{av} for plant-type Fd's as a function of $\Delta E/B$. The g_{av} shift (0.03) between ligands with and without carbonyl groups (Cys and SMe, respectively) is shown at the right. The important point is that the computed values of g_{av} (1.99–2.02) for plant-type Fd's (based on the 1CZP data) were too large, that is, the estimated ΔE_Ω value of 340 cm^{-1} was not sufficient to enforce electronic localization and decrease the g_{av} value. We therefore searched for other contributions to ΔE_{stat} in addition to ΔE_Ω.

Impact of the Solvent on g_{av} Values. Solvent issues are known to play a central role in determining the biophysical properties of proteins, including the iron−sulfur ferredoxins. For example, their redox potentials are very sensitive to solvent accessibility to the clusters,[96] through subtle changes in the charges of the sulfur atoms upon oxidation/reduction.[97–99] To this point, our calculations focused on the degree of localization/delocalization of the extra Fe 3d reducing electron between the two iron sites. These calculations were performed on the clusters in vacuo, whereas in the case of plant-type Fd's, the [2Fe−2S] clusters are known to be located near the protein surface and therefore close to the water solvent. Moreover, the reduced iron site in the WT proteins is Fe#1, which is closer to the protein surface, with (in the case of 1CZP) the Fe−Fe axis oriented roughly perpendicularly to that surface. Therefore, this Fe−Fe orientation maximizes the solvent-draining effect and may add to the trapping forces localizing the sixth ferrous d electron on Fe#1, as evidenced now. In contrast, it can be seen in Figure 5 that solvation issues do not play any role in determining g_{av} for WT Rieske centers already having large values (>4.5) of $\Delta E/B$.

The ferredoxin from the cyanobacterium *Anabaena* is roughly globular with a radius of 15 Å, and the reduced Fe#1 is located 5–6 Å from the surface. All of the data need not be very precise in order to illustrate the solvent effect semiquantitatively.

The ADF code relies on the COSMO approach[100–102] to quantitatively calculate solvation energies. Moreover, the present commercial ADF version allows only for two-layer modeling (but see the Summary and Conclusion for discussion of three-layer models). Given these constraints, we therefore constructed a pseudo-three-layer model by imbedding the [2Fe−2S](SMe)$_4$ cluster in a spherical cavity of radius $R = 15$ Å (i.e., the protein size) inside of which the dielectric constant was $\epsilon = 1$ (an actual protein would require $\epsilon \approx 4$). This cavity was itself immersed in an outside dielectric continuum having $\epsilon = 80$, representing water. This crude model was sufficient to semiquantitatively illustrate the importance of solvation effects. We varied the position of the cluster, which was originally placed at the center of the protein cavity (the coordinate z gives the distance between this center and Fe#1), having the cluster come close to and actually cross over the cavity surface. We computed the $\Delta E(\mathrm{HS})/B$ ratio at various cluster positions in order to see the impact of the expected charge-draining effect on the degree of electronic delocalization within the cluster as measured in the HS spin state.

We verified that when the cluster was moved toward the center of the cavity ($z \rightarrow 0$) or was moved away from the cavity well into the solvent ($z \rightarrow 30$ Å), the $\Delta E(\mathrm{HS})/B$ values were small (0.5). Therefore, in subsequent calculations, we assumed that $\Delta E_{solv} \approx \Delta E(\mathrm{HS}) - 0.5$. When the cluster was kept inside the cavity but moved close to the surface, the $\Delta E_{solv}/B$ ratio increased significantly, reaching a peak value of 6 [see Figure 6, in which $d_{(\mathrm{cluster/cavity})} = z$]. In the region $z =$

(96) Stephens, P. J.; Jollie, D. R.; Warshel, A. *Chem. Rev.* **1996**, *96*, 2491.
(97) Mouesca, J.-M.; Lamotte, B. *Coord. Chem. Rev.* **1998**, *178–180*, 1573.
(98) Mouesca, J.-M.; Chen, J. L.; Noodleman, L.; Bashford, D.; Case, D. A. *J. Am. Chem. Soc.* **1994**, *116*, 11898.
(99) Torres, R. A.; Lovell, T.; Noodleman, L.; Case, D. A. *J. Am. Chem. Soc.* **2003**, *125*, 1923.
(100) Klamt, A.; Schüürmann, G. *J. Chem. Soc., Perkin Trans.* **1993**, *2*, 799.
(101) Klamt, A.; Jones, V. *J. Chem. Phys.* **1996**, *105*, 9972.
(102) Klamt, A. *J. Phys. Chem.* **1995**, *99*, 2224.

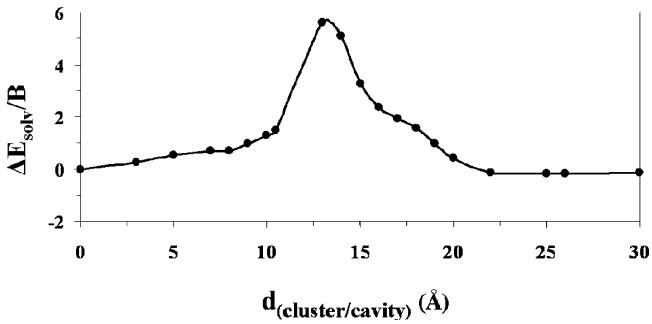

Figure 6. $\Delta E_{solv}/B$ ratio as a function of the position of the [2Fe−2S] cluster in the protein cavity [i.e., of the distance $d_{(cluster/cavity)}$ between Fe#1 and the center of the cavity]. Only converged calculations with sensible charge and spin distributions are reported.

11–12 Å, where the Fe#1 sulfur ligands cross the surface, the DFT calculations did not converge because the charge-draining effect became significant enough to cause the electronic charge distribution among the cluster atoms to become erratic. We can still expect that for [2Fe−2S] clusters in plant-type Fd's, the presence of the nearby solvent is sufficient to increase the $\Delta E_{solv}/B$ ratio by the one unit (for SMe ligands) or two units (for Cys ligands) needed to reach a g_{av} value of 1.96 (see Figure 5).

Exchange Coupling Constants for Ferredoxins and Rieske Proteins. The DFT J_{Heis} values for the oxidized (ox) and reduced (rd) redox states for both 1CZP (plant-type Fd) and 1JM1 (Rieske) model molecules are reported in Table 3 for the two XC potentials VBP and B3LYP. The VBP values are known to be too large. When we considered all of the J_{Heis} constants computed in this work, we found that $J_{Heis}(VBP) \approx 1.08J_{Heis}(B3LYP) + 252$ for the oxidized systems (with a correlation coefficient of 0.85) and $J_{Heis}(VBP) \approx 0.90J_{Heis}(B3LYP) + 345$ for the reduced systems (with a correlation coefficient of 0.91). Therefore, in what follows, only $J_{Heis}(B3LYP)$ values will be discussed.

The J_{Heis} values for both oxidized Fd and Rieske models are comparable, especially for the B3LYP potential (481 and 443 cm^{-1}, respectively). These values are in fair agreement with those measured experimentally: $J_{Heis}(Fd) \approx 366$ cm^{-1} [62,103] and $J_{Heis}(Rieske) \approx 360$ cm^{-1}.[59]

For the reduced state, in which the Rieske model is intrinsically valence-localized, it was expected that E_{Ferro} (see eq 8) would be intrinsically small. Indeed, we found $J_{eff}(Rieske) \approx 404$ cm^{-1}, and E_{Ferro} was computed to be –53 cm^{-1}. Additional solvation effects would only decrease the magnitude of E_{Ferro} and increase that of J_{eff} correspondingly (up to the maximum computed J_{Heis} value of 457 cm^{-1}). As for the g_{av} values (Figure 5), solvation has little impact on the electronic structure of a Rieske-type cluster, assuming that the histidine ligands remain protonated (see Section C below for the impact of deprotonation).

On the experimental side, Salerno et al.[60] reported a value of $J_{eff} = 130$ cm^{-1} for the Rieske protein in the mitochondrial cytochrome bc_1 complex, whereas for proteins in solution, Bertrand et al.[58] measured $J_{eff} = 200$ cm^{-1} for the *T. thermophilus* Rieske protein and $J_{eff} = 380$ cm^{-1} for the benzene dioxygenase enzyme from *P. putida*. J_{eff} values measured within a given class (here, Rieske centers with $g_{av} = 1.91$) vary drastically. Bertrand et al.[58] related such variations to the strains exerted on the cluster by the protein and therefore to the sulfur bridge geometry. However, keeping in mind that $J_{eff} = J_{Heis} + E_{Ferro}$, we suspect instead that J_{Heis} remains roughly constant for all Rieske clusters, whereas the magnitude of E_{Ferro} reflects the protein environmental factors. Among these are the location of the cluster relative to the protein surface (exposed or buried), solvent accessibility, protein dimerization (or even tetramerization) that might partially or totally shield the cluster from solvent, etc. All of these conditions lead to a great variation of E_{Ferro} and therefore J_{eff}. The main idea here is that the more solvent-exposed the cluster is, the larger is J_{eff} (with, again, a maximum value of 460 cm^{-1}). We will come back to these issues, which are not so easily sorted out, in the Summary and Conclusion of the present work.

The same observations can be made for plant-type versus adrenodoxin/putidaredoxin-type Fd clusters. Again, Salerno et al.[60] reported a very large J_{eff} value of 540 cm^{-1} for adrenal ferredoxin in intact mitochondria, whereas Bertrand et al.[58] found a J_{eff} value of "only" 340 cm^{-1} for the same protein in solution. For plant-type Fd's, experimental $J_{exp}(Fd)$ values are even smaller, reported to be in the range 150–200 cm^{-1} (see ref 61 and references therein). All of these values are significantly larger than our computed value based on the 1CZP PDB structure, $J_{eff}(Fd) \approx 31$ cm^{-1}, indicating that the ferromagnetic contribution (estimated as –382 cm^{-1} in Table 3) is too large. For example, to reach the experimental range of J_{eff} values for plant-type Fds, we need $E_{Ferro} \approx 230$–260 cm^{-1}, that is, $1 \leq \Delta E_{stat}/B \leq 2$ (see Figure S7 in the Supporting Information). The result that $\Delta E_{\Omega}/B = 0.5$ thus requires $0.5 \leq \Delta E_{solv}/B \leq 1.5$ for solvent effects. This range is compatible with what we obtained from the study of g_{av} for Fd's. The larger J_{eff} values measured for adrenodoxin-type clusters suggest a large intrinsic J_{Heis} term combined with large solvent accessibility.

To complete this study, we performed the same computation of J_{eff} for the case of the $[2Fe-2S](SCH_3)_4$ model of the C73S putidaredoxin from *P. putida* crystallized in the reduced redox state (PDB entry 1XLQ, resolution 1.45 Å).[51] Very interestingly, we found that $J_{Heis} = 695$ cm^{-1} and $J_{eff} = 300$ cm^{-1} without solvation effects (Table 3). The greater value of J_{Heis} was confirmed by the fact that for the double mutant (C73S, C85S) of the same reduced system at a lower resolution (1.84 Å, PDB entry 1XLO), we found $J_{Heis} = 652$ cm^{-1} (details not shown). The large value (540 cm^{-1}) reported by Salerno et al.[60] for the related adrenodoxin most probably corresponds to a solvated cluster, whereas that reported by Bertrand et al.[58] (340 cm^{-1}) is close to what we would propose for a solvent-shielded cluster.

We tried to explain the difference in the J_{Heis} values for 1CZP and 1XLQ in terms of structural parameters [Fe−Fe distance, S(Cys)−Fe−S(Cys) angle, Fe−S−Fe−S (inner core) dihedral angles, etc.] (including the other systems not discussed yet: clusters I and II of xanthine oxidases and the ferredoxin from *A. aeolicus*). It was not possible to relate

(103) Palmer, G.; Dunham, W. R.; Fee, J. A.; Sands, R. H.; Iizuka, T.; Yonetani, T. *Biochim. Biophys. Acta* **1971**, *245*, 201.

the difference to a single parameter. A more complete study of the exchange coupling in reduced [2Fe−2S](S-ligand)$_4$ clusters would involve full geometry optimizations (using the VBP XC potential) of broken symmetry states for various combinations of constrained Fe−Fe−S−C dihedral angles, Fe−Fe distances, and so on, followed by calculations of HS/BS bonding energy differences at the B3LYP level, in order to estimate the amplitude of the variations of J_{Heis}. Such a detailed study lies beyond the scope of the present work.

B. [2Fe−2S] Ferredoxins and Rieske Mutants. Plant-Type Ferredoxin Mutants. Let us start with the case of the Cys-to-Ser mutants of *Anabaena* [2Fe−2S] ferredoxin.[50] The cluster is attached to the proteic matrix through the following four cysteines: Cys41 and Cys46, attached to the (solvent-exposed) crystallographic Fe#1, and Cys49 and Cys79, attached to Fe#2. From an experimental point of view, the four mutants C41S, C46S, C49S, and C79S corresponding to the four successive ligands of the [2Fe−2S] cluster have been obtained, and their corresponding **g** tensors and g_{av} values have been measured by EPR in the reduced state (see Table 1). The first C41S mutant exhibits a small g_{av} value of 1.92, whereas the other three mutants present a common larger g_{av} value of 1.95, comparable to that of the H64C Rieske mutant. Noticing the poor stabilities of the C41S and C79S mutants in the reduced state at room temperature, the authors studied the two remaining C46S and C49S mutants by ^{1}H NMR spectroscopy.[50]

Temperature-dependent experiments aimed at discriminating between peaks with Curie and anti-Curie behavior were performed in order to identify the ferric and ferrous sites. In the first case (C46S), the reduced iron site was clearly Fe#1, ligating Cys41 and Ser46, as in the wild-type protein. In the second case (C49S), the authors could not identify the sites on the basis of the available NMR data.

From the 1CZP PDB file, we constructed three of the four [2Fe−2S](SCH$_3$)$_3$(OCH$_3$) models in which the OCH$_3$ ligand successively occupies each of the four cysteine positions (with a Fe−O distance of 2.00 Å). The exception was the C49S mutant, for which a crystallographic oxidized structure has been determined (PDB entry 1QOA, resolution 1.70 Å).[8] We did not optimize the geometries of the three models, as the X-ray crystal structure of the C49S mutant showed no significant change in the geometry of the cluster core when compared to that of the WT (1CZP) Fd. From a computational point of view, we noticed first that in all cases, on the basis of the HS states (eqs 3−5), the reducing electron was preferably located on the crystallographic Fe#1 site (the site closest to the solvent, bearing Cys41 and Cys46 in the WT structure).

Using the VBP XC potential, we computed ΔE(HS)/B ratios of 0.90, 0.72, 1.58, and 1.26 for C41S, C46S, C49S, and C79S, respectively (compared with the WT ratio of 1.03). The C46S result agrees with the NMR data concerning the location of the ferrous site (Fe#1). This was confirmed by computing (using the VBP XC potential) and comparing the energies of the BS1 and BS2 states. We found that E(BS1) − E(BS2) = 0.10, 0.13, 0.18, and 0.12 eV, respectively. This implies that the asymmetry introduced by the mutation (ΔE_{chem}) is (surprisingly) smaller than what could be achieved through ligand orientation (ΔE_{Ω}) (see Figure 4). In all cases of one- versus two-ligand substitution considered in the present study, we observed that the ΔE_{chem} term was not additive. The iron site energies were scarcely affected upon replacement of only one sulfur (second-row) ligand by a nitrogen or oxygen (first-row) ligand.

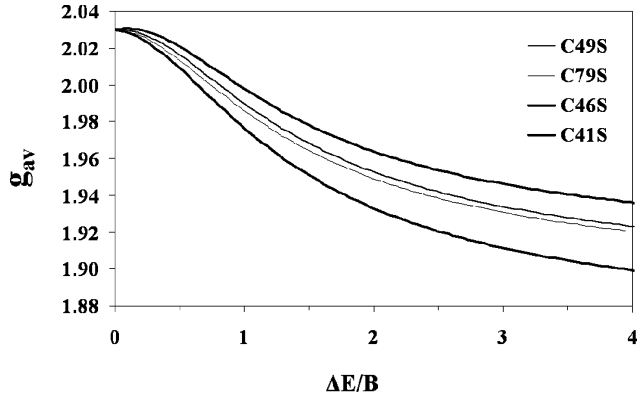

Figure 7. Values of g_{av} for plant-type ferredoxin mutants as a function of $\Delta E/B$.

Table 4. Values of g_{av} for the Four Cys → Ser Mutant Models [2Fe−2S](SCH$_3$)$_3$(OCH$_3$)

mutant	g_a(BS1)	g_b(BS2)	ΔE(HS)/B	g_{av}	g_{av} (+ solvent)[c]
C41S[a]	1.860	1.877	0.90	1.981	1.912
C46S[a]	1.902	1.878	0.72	1.996	1.949
C49S[b]	1.896	1.887	1.58	1.965	1.927
C79S[a]	1.896	1.898	1.26	1.974	1.927

[a] Based on the 1CZP crystallographic structure. [b] Based on the 1QOA crystallographic structure. [c] Solvent offset: $\Delta E_{solv}/B = 2.0$.

The corresponding BS **g** tensors (with ferrous Fe#1 and ferric Fe#2) were 1.860, 1.902, 1.896, and 1.896, respectively (see Table 4). It can be seen in Figure 7 that comparable solvent contributions clearly separate the smaller g_{av} value for C41S (computed as 1.91 for $\Delta E/B \approx 2.5$) from the other three larger values (1.93–1.95 for $\Delta E/B$ in the range 2.0–3.0), as observed experimentally by EPR. In other words, as far as the value of g_{av} is concerned, the key feature distinguishing C41S from the other three mutants is the local ferrous **g** tensor (1.86), which is significantly smaller than the other three local tensors (1.90; see Table 4). It can be verified that this differential effect is mainly due to a change in the ferrous electronic structure in BS states: the weight of the d_{xy} orbital in the HOMO of C41S (57%) is significantly greater than that in all three others (41–43%) (see ref 48). Only a large solvation contribution can manifest that electronic difference.

It should be noted that in Table 1, we only reported the main **g**-tensor components for the four mutants. It has been reported by the authors of the EPR study that the Cys → Ser mutants showed additional smaller g_2 principal values: 1.91 for C41S, 1.95 for C46S, 1.92 for C49S, and 1.93 for C79S. Some of the mutants (C46S and C79S) even exhibited several turning points in their spectra, indicating that the samples were heterogeneous. Such structural heterogeneities were introduced by freezing of the samples, as they did not

Table 5. Exchange Coupling Constants for the Four Cys → Ser Mutants of the [2Fe−2S] Cluster from the *Anabaena* Ferredoxin[a]

	C41S		C46S		C49S		C79S	
	VBP	B3LYP	VBP	B3LYP	VBP	B3LYP	VBP	B3LYP
J_{Heis}(ox)	736	456	754	470	735	454	749	464
B	722	(480)	728	(476)	672	(449)	684	(456)
ΔE(HS)	650	(868)	520	(854)	1060	(983)	865	(909)
E_{Ferro}[b]	−408		−433		−304		−344	
E_{Ferro} (+ solvent)[c]	+189		+201		+132		+155	
J_{Heis}(rd)	559	228	707	309	645	324	665	330
J_{eff}	151	−180	274	−124	341	20	321	−14
J_{eff} (+ solvent)[c]	340	9	475	77	473	152	476	141
$\varepsilon_{9/2} - \varepsilon_{1/2}$	39		926		1620		1535	
$\varepsilon_{9/2} - \varepsilon_{1/2}$ (+ solvent)[d]	778		1672		2253		2211	

[a] All values in cm^{-1}. [b] Computed from eq 8 with the VBP values. [c] Solvent offset: $\Delta E_{solv}/B = 2.0$. [d] Energy difference estimated as $12J_{Heis} - (\Delta E^2 + 25B^2)^{1/2} + (\Delta E^2 + B^2)^{1/2}$ (see Scheme 2 and eq 7a).

appear in NMR spectra at room temperature.

We also computed J_{eff} exchange coupling constants for the four mutants (Table 5). In view of the fact that the reducing electron favorably localizes on the solvent-exposed Fe#1 site, the J_{eff} values for the C41S and C46S mutants (Fe#1 ligands) were clearly ferromagnetic and large (−180 and –124 cm^{-1}, respectively), whereas for the C49S and C79S mutants (Fe#2 ligands), the J_{eff} values were small (20 and –14 cm^{-1}, respectively).

The relative decrease in the J_{eff} values for the first two mutants is related to that of the Heisenberg values (228 and 309 cm^{-1}, respectively) compared with those for C49S and C79S (324 and 330 cm^{-1}, respectively; see Table 5) and the WT (413 cm^{-1}; see Table 3). As in the case of the experimental g_{av} values, the C41S mutant is distinguished from the other three mutants by a smaller J_{Heis} constant. The $\varepsilon_{9/2} - \varepsilon_{1/2}$ energy difference, estimated using eq 7a as $12J_{Heis} - (\Delta E^2 + 25B^2)^{1/2} + (\Delta E^2 + B^2)^{1/2}$, is very small (39 cm^{-1}) for this C41S mutant. More generally, the magnitude of J_{Heis} diminishes when the reducing electron is located near the oxygen ligand. Assuming the same solvent contribution as for the WT ($\Delta E_{solv}/B \approx 2$), which reduces the magnitude of the ferromagnetic contribution, we obtained J_{eff}(C41S) ≈ 9 cm^{-1} and J_{eff}(C46S) ≈ 77 cm^{-1}. These values are most probably still too small. But the main idea here is that a large trapping term (in this case due to the solvent) stabilizes the $S = {}^1/_2$ over the $S = {}^9/_2$ state. We conclude this section on plant-type Fd mutants by observing that the $S = {}^9/_2$ state lies far above the $S = {}^1/_2$ ground state because of the large solvation effect.

Rieske Mutants. The (unstable) H64C mutant of the Rieske-type [2Fe−2S] cluster from *S. solfataricus* showed a nearly axial EPR signal with $g_{av} \approx 1.947$.[13] We constructed various mutant models based on the reduced 1JM1 structure (see Table 6) and computed ΔE(HS)/B ratios in vacuo. At this level, ΔE(HS) contained the effective vibronic and ligand-orientation terms. It can be verified first that the computed g_{av} values (1.96–1.97) were intermediate between those computed for plant-type Fd (1.99–2.02) and Rieske (1.89–1.91) models, as expected. This can be verified also in Figure 5. The systems modeling (in vacuo) the H64C mutation resulted in small ΔE(HS)/B ratios (1), having become sensitive to solvent exposure. A small increase of 0.5 in $\Delta E_{solv}/B$ would be sufficient to reach the target value of 1.947.

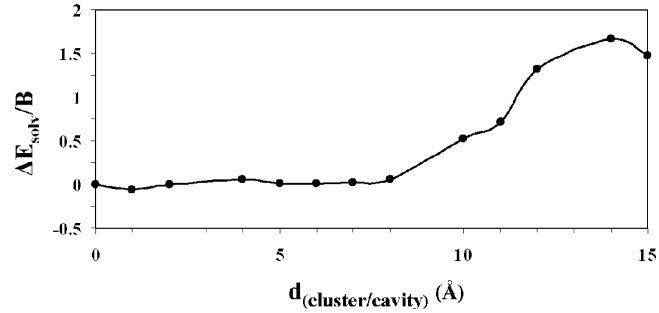

Figure 8. $\Delta E_{solv}/B$ ratio as a function of the Rieske [2Fe−2S] cluster position in the cavity [i.e., of the distance $d_{(cluster/cavity)}$ between Fe#2 and the center of the cavity]. Here, $B \approx 700$ cm^{-1} and $\Delta E_{solv}/B = \Delta E$(HS)/$B$ − ΔE(HS)/B($d = 0$) (see main text).

Table 6. Values of g_{av} for Rieske Mutant Models Having Various (S_3N) Ligand Combinations

ligands						
Fe#1	Fe#2	g_a(BS1)	g_b(BS2)	ΔE(HS)/B	g_{av}	g_{av} (+ solvent)[a]
$(SCH_3)_2$	(Imid)(SCH_3)	1.873	1.856	1.22	1.962	1.941
$(SCH_3)_2$	(His)(SCH_3)	1.873	1.873	1.31	1.968	1.949
$(Cys)_2$	(Imid)(Cys)	1.879	1.837	0.92	1.971	1.943
$(Cys)_2$	(His)(Cys)	1.879	1.837	0.86	1.974	1.943

[a] Solvent offset: $\Delta E_{solv}/B = 0.5$.

Using the same conditions as for plant-type Fd models, we computed $\Delta E_{solv}/B$ ratios for the [2Fe−2S]$(SCH_3)_3$(Imid) model as a function of its distance from the cavity center (15 Å cavity radius). Interestingly, all things being equal, the localization of the reducing electron was less pronounced than for the Fd's, having a maximum value of 1.7 (see Figure 8).

C. Deprotonated Rieske Centers and Xanthine Oxidases. Deprotonated Rieske Centers. Starting from the 1JM1 structure,[92] we deprotonated the two imidazole or histidine ligands (depending on the model). We computed local BS **g** tensors and the resulting g_{av} values as a function of ΔE(HS)/B for two models: $(SCH_3)_2$[2Fe−2S](Imid-deprot)$_2$ and $(Cys)_2$[2Fe−2S](His-deprot)$_2$.

One striking feature was the result that deprotonation of the imidazole rings significantly reduced the ΔE(HS)/B ratio (0.9) compared with the protonated Rieske value of 4.5 (see Table 3). At this level, the ΔE(HS) term contained the effective vibronic contribution and ligand effects (conformation and chemical nature). This behavior was previously noticed by Noodleman and Han.[104] Their DFT computations showed that ΔE, defined by the authors as the site-trapping energy and containing vibronic and site-inequivalence energy terms, was greatly reduced upon increasing the pH from 7 to 14, that is, to pH values where both histidine ligands become deprotonated.

The g_{av} value we computed for the realistic model (Cys + His-deprot) was 1.96 (1.97 for SCH_3 + Imid-deprot), which is equal to the value measured experimentally. However, solvent effects were not included in this calculation, and we knew that their inclusion would decrease this

(104) Noodleman, L.; Han, W.-G. *J. Biol. Inorg. Chem.* **2006**, *11*, 674.

Table 7. Spin Hamiltonian Parameters for the Rieske Cluster Model with Deprotonated Imidazole Ligands[a]

parameter	value	
	VBP	B3LYP
J_{Heis}(ox)	724	432
B	588	(491)
ΔE(HS)	538	(491)
E_{Ferro}	−330	
E_{Ferro} (+ solvent)[b]	+57	
J_{Heis}(rd)	533	330
J_{eff}	203	0
J_{eff} (+ solvent)[b]	276	57
J_{eff} (exp)	43	

[a] Based on the 1JM1 PDB file. Ligands: Fe#1, $(SCH_3)_2$; Fe#2, $(Imid\text{-}deprot)_2$. [b] Solvent offset: $\Delta E_{solv}/B = 0.5$.

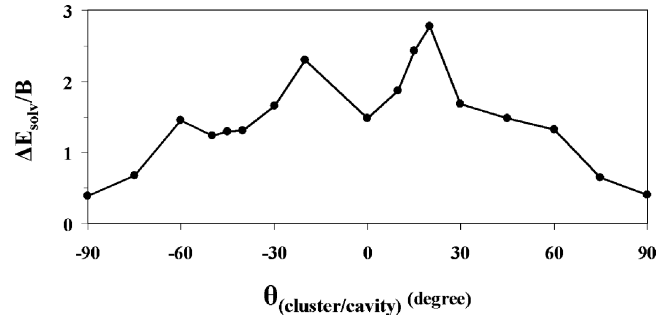

Figure 9. $\Delta E_{solv}/B$ ratio as a function of the XO [2Fe−2S] cluster II orientation in the cavity (i.e., of the angle between the Fe−Fe axis and the vector normal to the surface of the cavity). When $\theta = 0°$, the closer iron atom is located 5 Å from the cavity surface. The globular 1VLB protein is modeled as a sphere having a radius of 20 Å.

g_{av} value to an unknown value $g_{av}°$.

In order to explain the difference between $g_{av}°$ and 1.96, de Oliveira et al.[56] took into account the antisymmetric Dzyaloshinsky−Moriya (ADM) exchange mechanism[105–107] that mixes the excited $S = {}^3/_2$ state into the $S = {}^1/_2$ ground spin state. The ADM term $\mathbf{d}_{AB}\cdot\hat{\mathbf{S}}_A \times \hat{\mathbf{S}}_B$ must be included in order to explain the observed broadening of the EPR lines. de Oliveira et al. equated $g_{av}°$ with 1.91, the WT Rieske value. Therefore, the d_{AB}/J_{eff} ratio they determined (0.18) most probably represents an upper limit (in which case, $|d_{AB}| \approx 8$ cm^{-1}). From a phenomenological point of view, the ADM mechanism is relevant when the effective exchange coupling constant J_{eff} is sufficiently small. As reported in Table 7, we computed a J_{eff} value of 0 cm^{-1}, to be compared with experiment (43 cm^{-1}).

This small value was essentially due to a large ferromagnetic contribution (−330 cm^{-1}), that is, a small ΔE(HS) value. For this analysis to hold, the solvation term must play a minor role, as it decreases g_{av} and increases J_{eff} at the same time. This was consistent with what we found above for the H64C Rieske mutant, since with $\Delta E_{solv}/B = 0.5$, we then found $J_{eff} \approx 57$ cm^{-1} and $g_{av}° \approx 1.925$ (i.e., $|d_{AB}| \approx 5$ cm^{-1})

Xanthine Oxidase Family. We constructed our models from the oxidized enzyme structure (PDB entry 1VLB; resolution 1.28 Å).[93] In Table 8, we report g_{av} values. It can be seen that clusters I and II are very similar from this point of view.

In contrast to the plant-type Fds, no additional solvation effect is expected in the case of cluster I, which is deeply buried in the protein matrix. Our results agreed with the experimental range of 1.95–1.97.[55] Cluster II is solvent-exposed, but the orientation of the Fe−Fe z axis is roughly parallel to the protein surface, whereas in Fd's, it was perpendicular to the surface. We checked the effect of the cluster orientation (from –90° to 90° with respect to the vector normal to the surface) on the $\Delta E_{solv}/B$ solvation term (see Figure 9). It is noteworthy that each of the two maximum values (at $\theta \approx \pm 20°$) was reached when the Fe−SMe bond was nearly perpendicular to the cavity surface. For $\theta \approx \pm 90°$, the $\Delta E_{solv}/B$ ratio was minimal, as anticipated.

The key observation concerning the XO distal clusters II is that the measured g_{av} values[55] are in the range 1.95–1.97, in contrast to the computed values of 1.97–2.01. The antisymmetric exchange term $\mathbf{d}_{AB}$ seemed to be inactive in clusters I but caused the g_{av} values of clusters II to increase by as much as 0.05. This was at first intriguing, as the value of g_{av} for cluster I matched that of the plant-type Fd's (1.96), whereas from a conformational point of view (i.e., the Fe−Fe−S−C_β dihedral angles), clusters II resemble the plant-type Fd's.

While looking for some peculiar geometrical feature of the proximal clusters I, we noticed that they exhibit nearly centrosymmetric [2Fe−2S](SC_β) cores. This fact should be sufficient to cancel (to first order) the antisymmetric exchange vector $\mathbf{d}_{AB}$. Moreover, the B3LYP J_{eff} values computed for clusters I of 1VLB ($J_{eff} \approx 135$ cm^{-1}) and 1FO4 ($J_{eff} \approx 110$ cm^{-1}) were large and similar to values for plant-type Fd's ($J_{eff} \approx$ 150–200 cm^{-1}) (see Table 9).

In contrast, the departure of g_{av} from 1.96 for clusters II may reflect the variation of the d_{AB}/J_{eff} ratio (through that of E_{Ferro}). Both plant-type Fd's and XO clusters II present very similar Fe−Fe−S−C_β dihedral angles, and therefore most probably have a similar range of d_{AB} values. In the case of the plant-type Fd's, however, as already stated above, the nearby solvent substantially increases the $\Delta E/B$ ratio and therefore the J_{eff} value, thus damping the effect of the antisymmetric term. Such is not the case for XO clusters II.

It is therefore interesting to compare computed J_{eff} values for clusters I and II for two XO-type proteins. The first one (*D. gigas* aldehyde oxidoreductase, PDB entry 1VLB) exhibits close g_{av} values for the two clusters: g_{av}(cluster I) $\approx$ 1.959 and g_{av}(cluster II) $\approx$ 1.976. The second one (xanthine dehydrogenase from bovine milk, PDB entry 1FO4)[94] shows different g_{av} values: g_{av}(cluster I) $\approx$ 1.952 and g_{av}(cluster II) $\approx$ 2.005.

As can be seen in Table 9 for clusters II, the d_{AB}/J_{eff} ratio was damped for 1VLB because of a large J_{eff} value. However, the substantial decrease in J_{eff}(cluster II) in going from 1VLB (208 cm^{-1}) to 1FO4 (−13 cm^{-1}), which was mainly due to a larger E_{Ferro} contribution, should also be noted. This is in line with the corresponding increase of the cluster II g_{av} values from 1.976 (1VLB) to 2.005 (1FO4)

(105) Moriya, T. In *Magnetism*; Rado, G. T., Suhl, H., Eds.; Academic Press: London, 1963; Vol. *1*, p 91.
(106) Moriya, T. *Phys. Rev.* **1960**, *120*, 91.
(107) Dzyaloshinsky, I. *J. Phys. Chem. Solids* **1958**, *4*, 241.

Table 8. Values of g_{av} for the XO [2Fe−2S] Cluster I and Cluster II from 1VLB

cluster	ligands	g_a (BS1)	g_b (BS2)	ΔE(HS)/B	g_{av}	g_{av} (+ vibronic)[a]
cluster I (proximal)	$(SCH_3)_2(SCH_3)_2$	1.879	1.876	1.11	1.980	1.957
	$(Cys)_2(Cys)_2$	1.919	1.896	0.94	2.005	1.985
cluster II (distal)	$(SCH_3)_2(SCH_3)_2$	1.882	1.880	0.82	1.996	1.972
	$(Cys)_2(Cys)_2$	1.919	1.896	0.94	2.005	1.985

[a] Values include a common vibronic offset of $\Delta E_{vib}^{eff}/B = 0.5$.

via an ADM-type mechanism. In the case of 1FO4 cluster II, we missed the expected experimental value (40–45 cm^{-1}) by a small amount.

The ADM term of the form $\mathbf{d}_{AB}\cdot\hat{\mathbf{S}}_A \times \hat{\mathbf{S}}_B$ mixes valence-localized Heisenberg spin states in which the extra electron is located on the same metal site: in our notation, the ADM exchange term mixes $\Psi_a(S, M_S)$ and $\Psi_a(S-1, M_S \pm 1)$. Applied to the case of the reduced [2Fe−2S] cluster, this ADM mechanism allows for the admixture of the $\Psi_a(^3/_2, ^3/_2)$ and $\Psi_a(^3/_2, -^1/_2)$ states (where Ψ_a corresponds to $[Fe^{3+}-Fe^{2+}]$) into the $\Psi_a(^1/_2, ^1/_2)$ doublet ground state.

In a recent series of papers, Belinsky[108–112] has shown the value of introducing antisymmetric double-exchange (ADE) into the spin Hamiltonian pertaining to mixed-valence clusters. This ADE mechanism combines a spin–orbit-coupled mixture of ground and excited states of the ferrous ion with an electron transfer between iron sites. The corresponding spin Hamiltonian, formulated as $2i\mathbf{K}_{AB}\cdot\mathbf{T}_{AB}\cdot(\hat{\mathbf{S}}_B - \hat{\mathbf{S}}_A)$, contains a spin-flip hopping vector transfer, $\mathbf{K}_{AB}$, as the antisymmetric vector coefficient. One key requirement for this mechanism to operate is a distortion of the [2Fe−2S] core, breaking the mirror-plane symmetry relating the two metal sites (this ADE term is further discussed in Appendix B). The ADE term mixes valence-localized Heisenberg spin states having different electron localizations, that is $\Psi_a(S, M_S)$ can be mixed with either $\Psi_b(S, M_S \pm 1)$ or $\Psi_b(S-1, M_S \pm 1)$ (where Ψ_b corresponds to $[Fe^{2+}-Fe^{3+}]$). Belinsky has treated the specific case of fully delocalized mixed-valence $[Fe^{2.5+}-Fe^{2.5+}]$ clusters, in which the isotropic double-exchange parameter B is dominant and results in the $S = ^9/_2$ ground state, for which $[c_a(S)]^2 = [c_b(S)]^2 = ^1/_2$.

In line with the general framework of the present study, we have also briefly treated the case of an $S = ^1/_2$ ground spin state with intermediate electronic localization/delocalization. It is shown in Appendix B that unless the [2Fe−2S] system is extremely localized, the ADE mechanism dominates over the ADM mechanism. Therefore, Belinsky's ADE term is most probably the one that causes the broadening of the EPR lines in XO clusters II and the deprotonated Rieske cluster. Still, the ADE and ADM mechanisms are phenomenologically equivalent.

(108) Belinsky, M. I. *Inorg. Chem.* **2006**, *45*, 9096.
(109) Belinsky, M. I. *Chem. Phys.* **2006**, *325*, 313.
(110) Belinsky, M. I. *Chem. Phys.* **2006**, *325*, 326.
(111) Belinsky, M. I. *Chem. Phys.* **2005**, *308*, 27.
(112) Belinsky, M. I. *Chem. Phys.* **2003**, *288*, 137.

Table 9. Exchange Coupling Constants for XO [2Fe−2S] Clusters I and II

	1FO4				1VLB			
	cluster I		cluster II		cluster I		cluster II	
	VBP	B3LYP	VBP	B3LYP	VBP	B3LYP	VBP	B3LYP
J_{Heis}(ox)	794	505	824	519	732	470	760	477
B	596	(539)	731	(669)	687	(624)	625	(556)
ΔE	528	(689)	11	(204)	764	(848)	511	(840)
E_{Ferro}	−338		−487		−363		−362	
E_{Ferro} (+ vibronic)[a]	+55		+34		+60		+58	
J_{Heis}(rd)	660	392	774	440	641	438	813	512
J_{eff}	322	55	287	−47	278	75	451	150
J_{eff} (+ vibronic)[a]	377	110	321	−13	338	135	509	208
g_{av} (exp)	1.952		2.005		1.959		1.976	

[a] Values include a common vibronic offset of $\Delta E_{vib}^{eff}/B = 0.5$.

D. Mutated Forms of the [2Fe−2S] Ferredoxin from *C. pasteurianum* and *A. aeolicus*. The primary structures of the two otherwise-similar Fd's from *C. pasteurianum* (Cp) and *A. aeolicus* (Aa) are not related to any other plant-type Fd protein sequence.[9,52,113,114] They belong to the (vertebrate) thioredoxin-like family of Fd's and are unique because of the unusual distribution of their five cysteines in the amino-acid sequences. No three-dimensional crystallographic structures are available to date for these WT proteins in their reduced states. However, the oxidized protein of the Aa WT Fd and its C55S and C59S mutants (Cys 55 and Cys59 are the ligands of the solvent-exposed Fe#2; the ligands of Fe#1 are Cys9 and Cys22) have been crystallized at high resolution (1.50, 1.25, and 1.05 Å, respectively). The C55S and C59S structures are especially valuable when considering the counterpart C56S and C60S variants of the homologous protein from Cp. In effect, EPR studies of both Cp mutants reveal a mixture of clusters having either $S = ^1/_2$ or $S = ^9/_2$ ground states.[15,23]

From the point of view of the present study, we notice first that EPR spectra of the Cp WT protein yielded three **g**-tensor components (2.004, 1.948, and 1.922) whose average value is $g_{av} = 1.96$, as for the plant-type Fd's and XO clusters I. Three cysteine ligands have been successively replaced by serines, yielding the C11S, C56S, and C60S mutants. The g_{av} value for C11S is 1.96, as in the WT. For C56S and C60S, the authors measured g_{av} values of 1.935 and 1.937, respectively,[54] which are intermediate between 1.91 and 1.96.

We performed **g**-tensor computations on the WT as well as on the C55S and C59S mutants of the Fd from *A. aeolicus* (keeping the cysteine ligands or replacing them by SCH_3 ligands). In both WT models, the reducing electron clearly localized on the solvent-exposed Fe#2. Our computed g_{av} values (see Table 10) strongly suggested that no additional solvent (trapping) contribution was needed to reach the experimental value. This is due to the already large $\Delta E_Q/B$ ratio (1.5, to which an effective vibronic contribution had to be added) as compared with 0.5 for the reduced 1CZP

(113) Golinelli, M. P.; Akin, L. A.; Crouse, B. R.; Johnson, M. K.; Meyer, J. *Biochemistry* **1996**, *35*, 8995.
(114) Chatelet, C.; Gaillard, J.; Pétillot, Y.; Louwagie, M.; Meyer, J. *Biochem. Biophys. Res. Commun.* **1999**, *261*, 885.

Table 10. Values of g_{av} for the Three Models of Aa (Oxidized WT and C55S and C59S Mutants)[a]

model	ligands Fe#1	ligands Fe#2	g_a(BS1)	g_b(BS2)	ΔE(HS)/B	g_{av}	g_{av} (+ vibronic)[b]
WT	$(SCH_3)_2$	$(SCH_3)_2$	1.897	1.897	1.48	1.971	1.956
WT	$(Cys)_2$	$(Cys)_2$	1.939	1.934	1.21	1.994	1.982
C55S	$(SCH_3)_2$	$(OCH_3)(SCH_3)$	1.897	1.887	0.36	2.019	1.990
C59S	$(SCH_3)_2$	$(SCH_3)(OCH_3)$	1.897	1.884	0.33	2.020	1.990
C55S	$(Cys)_2$	(Ser)(Cys)	1.939	1.951	0.72	2.018	2.004

[a] The models were based on the 1M2A, 1M2B, and 1M2D PDB files, respectively. [b] Values including a common vibronic offset of $\Delta E_{vib}^{eff}/B = 0.5$.

model. The difference arises from different ligand conformations (see Figure 4). In effect, two nearly equal Fe−Fe−S−C_β angles (−8° and –26° in the oxidized structure) are associated with the Fe#2 site of Aa (Cp). The Fe#1 site of Aa (Cp) is in turn analogous to that of Fe#1 in plant-type Fd's, with angles of –126° and –133°. As can be seen in Figure 4, for $\Omega_1 = \Omega_2 \approx 120°$, the opposite site at $\Omega_3 = \Omega_4 \approx 0°$ is more stable by $\Delta E_\Omega/B \approx 1.5$.

Moreover, we noted that the Arg13 residue in the Aa WT structure can adopt two different conformations ("closed" and "open"). In the (major) closed conformation, the guanidino moiety donates a hydrogen bond to the Cys59 S_γ atom, whereas in the (minor) open conformation, this group is oriented in such a way as to cancel any interaction between the 13 and 59 residues. In the WT structure, the closed conformation allows Arg13 to shield the [2Fe−2S] cluster from the solvent, in line with our computations suggesting that solvation plays a minor role in the WT (assuming that such a closed conformation is conserved upon cluster reduction).

For the C55S (Cys and SMe) and C59S (SMe) mutant models, the computed $\Delta E/B$ ratios were very small. Even taking into account an additional effective vibronic coupling of 0.5B was not nearly sufficient to reproduce the experimental g_{av} values. We needed an additional solvent contribution of $\Delta E_{solv}/B \approx 1.5$, which is of the same order as that required to explain the plant-type mutant data (see Section A of the Results and Discussion). Again, this matches what has been observed for the C55S and C60S crystallographic structures when the side chain of Arg13 adopts the open conformation. In those cases, a water molecule forms a hydrogen bond to the Cys59 S_γ/O_γ atom in place of the Arg13 guanidino group. In other words, the [2Fe−2S] cluster becomes solvent-exposed.

The above rationalization of the g_{av} values measured by EPR for the reduced WT and the C55S and C69S mutants of Cp, developed with the help of the Aa oxidized crystallographic structure, allows us to conclude that conformational changes (open vs closed) around the Fe#2 site play a major role in determining the spectroscopic features of these [2Fe−2S] clusters. Such a distribution of protein conformations has also been invoked in order to explain temperature-dependent valence delocalization in the reduced [2Fe−2S] clusters of WT and C56S Cp, as observed by Mössbauer and magnetization studies. In effect, samples of the C56S variant contain a mixture of clusters with valence-localized $S = {}^1/_2$ and valence-delocalized $S = {}^9/_2$ ground states. Moreover, high-temperature Mössbauer studies revealed an increase in the fraction of valence-delocalized clusters without spin conversion from $S = {}^1/_2$ to $S = {}^9/_2$ spin states (which was ruled out by magnetic susceptibility studies[15,23]). It was then shown that a rapid increase in the intramolecular electron-transfer rate between the two iron sites results from a distribution of the magnetic parameters (superexchange, double-exchange, and vibronic terms), a distribution matching that of the protein conformations. We now illustrate the impact of this observation on the computed values of the effective magnetic parameters.

We start our analysis with a plot of the (J_{Heis}, ΔE_{stat}) combinations for which the energies of the $S = {}^1/_2$ and $S = {}^9/_2$ states become equal (see Figure 10, drawn using the exact eq 16c). In the upper-right portion of the plot, $S = {}^1/_2$ is the ground state, while $S = {}^9/_2$ is the ground state in the lower-left portion). To obtain an $S = {}^9/_2$ ground state, two conditions must be realized: (i) the J_{Heis} value must be substantially decreased (below 240 cm^{-1}) from the standard value of >400 cm^{-1} usually computed for [2Fe−2S] clusters with sulfur ligands; and (ii) the total of the trapping terms (ligand conformation + effective vibronic + solvent, etc.) must be moderate (this condition is less strict the smaller J_{Heis} is). For the Cys → Ser mutants of the *Anabaena* Fd, we already verified that the ligand substitution resulted in the expected decrease (between 230 and 330 cm^{-1}) in the computed J_{Heis} values. However, due to a substantial solvent effect, the ground state was $S = {}^1/_2$ in that case.

We therefore computed the exchange coupling constants J_{Heis} and J_{eff} for the WT and the C55S and C59S mutants (see Table 11). For our 1M2A-based model, we found a quite large value of the coupling constant J_{Heis} (600 cm^{-1}) that resulted, however, in a standard J_{eff} value of 265 cm^{-1}. No further significant solvent antiferromagnetic contribution is expected, for reasons already explained above (the cluster is most probably shielded from the solvent in the WT closed conformation).

For both mutants (especially C55S), we obtained J_{Heis} values having relatively small magnitudes, although not as small as expected. The J_{eff} values were negative, which in this context means only that the $S = {}^3/_2$ state is lower than the $S = {}^1/_2$ state but not necessarily that the $S = {}^9/_2$ state is the ground state. We think that upon reduction, the [2Fe−2S] cluster may experience enough conformational changes to alter our present results, which are based on the oxidized and open structures. For example, when we optimized the geometries of the C55S and C59S models in the BS state (with the reducing electron on the mutated iron site), we computed J_{Heis} values of 131 and 163 cm^{-1}, respectively. These values are precisely those predicted from the B and ΔE(HS) values in Table 11 for the $S = {}^1/_2 \leftrightarrow S = {}^9/_2$

Table 11. Exchange Coupling Constants for the WT and Related Mutants of the Aa Fd

	1M2A		1M2B		1M2D	
	VBP	B3LYP	VBP	B3LYP	VBP	B3LYP
J_{Heis}(ox)	735	461	760	474	721	452
B	711	(650)	673	(469)	717	(499)
ΔE(HS)	1056	(1111)	244	(21)	237	(18)
E_{Ferro}	−332		(−435)		(−466)	
J_{Heis}(rd)	874	597	592	244	666	308
J_{eff}	542	265	(157)	(−191)	(200)	(−158)
$\varepsilon_{9/2} - \varepsilon_{1/2}$[a]	5016		270/−1086[b]		834/−882[b]	

[a] Estimated as $12J_{Heis} - (\Delta E^2 + 25B^2)^{1/2} + (\Delta E^2 + B^2)^{1/2}$ (see Scheme 2). [b] With $J_{Heis} = 131$ cm^{-1} (1M2B) and 163 cm^{-1} (1M2D) (see main text).

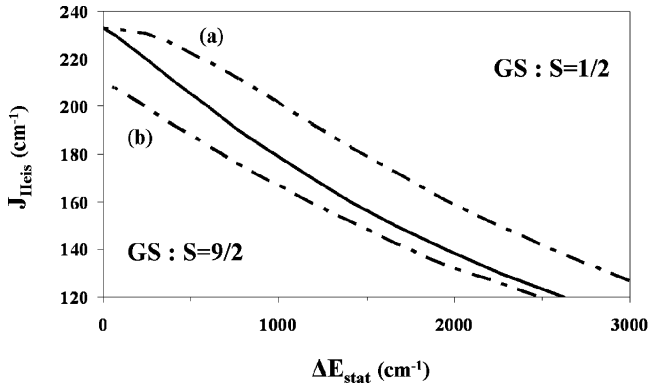

Figure 10. Plot of values of J_{Heis} for which the $S = {}^1/_2$ and ${}^9/_2$ states are degenerate as a function of ΔE_{stat} (obtained using eq 16c). Dotted lines show curves obtained from eq 7a with (a) vibronic offset = 0 cm^{-1} and (b) vibronic offset = 800 cm^{-1} and $B = 700$ cm^{-1}.

transition.

The important point is that both mutants of Aa (and Cp) most probably exist in solution or in vivo in two conformations (only the open one is crystallized in the oxidized state, as discussed above). From Figure 10, given a common moderate value of J_{Heis} in the two conformations, the open conformation exposes the cluster to solvent, resulting in the $S = {}^1/_2$ ground state. In contrast, the closed conformation yields a small overall static trapping term, thus allowing for an $S = {}^9/_2$ ground spin state. Moreover, a small static term is required (see Figure 1), as the study of the $S = {}^9/_2$ ground spin state by Mössbauer techniques revealed that this state is nearly fully delocalized.

Summary and Conclusions

In this DFT theoretical study, we have tried to construct a unified phenomenological framework rationalizing the distribution of the **g**-tensor average values g_{av} and effective exchange coupling constants J_{eff} measured for a wide set of typical protein systems, including plant-type Fd's and Rieske proteins (and related mutants), the deprotonated Rieske center at pH 14 (R14), XO clusters I and II, and the unusual Cp (and Aa) thioredoxin-like Fd whose [2Fe−2S] cluster exhibits a mixture of clusters with $S = {}^1/_2$ or $S = {}^9/_2$ ground states.

The key quantity in our analysis is the ratio $\Delta E/B$ indexing the relative strengths of the trapping forces (which favor electronic localization) on the one hand and the double-exchange term (which favors electronic delocalization) on the other. At the XC-VBP level, we consistently found B values in the range 600–700 cm^{-1}. Total ΔE values (including vibronic, ligand-conformation, and solvation terms) were as large as $3B$, except for the Rieske centers, which as a result of a large ΔE_{chem} offset had $\Delta E/B$ values of >4.5 (see Table 2).

Among the intrinsic contributions to ΔE, we first showed how the vibronic term ΔE_{vib} appears in the form of an effective value ΔE_{vib}^{eff} varying between 0 and ΔE_{vib}, depending on the relative strength of B versus all of other trapping forces combined (i.e., ΔE_{stat}). This term, especially the vibronic coupling λ, was the most difficult to compute because of the peculiar structural behavior of BS states. We tried to extract a value of ΔE_{vib} from experimental data pertaining to the *Anabaena* Fd and found it to lie in the range 800–900 cm^{-1}, which is only half the values usually proposed (1600 cm^{-1}). For large values of ΔE_{stat}, ΔE_{vib}^{eff} reached its maximum value ΔE_{vib} and contributed to valence trapping at the same level as the other terms (see eq 7a and also eqs 15e and 16c).

Because the ΔE_{vib} value derived from monomer data (1600 cm^{-1}) is twice the value we used in all of the plots in this paper, in Figure S7 in the Supporting Information we have compared the exact J_{eff} curves (obtained using eqs 16a,c) for "small" (800 cm^{-1}) and "large" (1600 cm^{-1}) values of ΔE_{vib}. It can be seen that in the latter case, J_{eff} is always larger than 100 cm^{-1}. This caused some problems in reproducing the experimental J_{eff} range for deprotonated Rieske centers and XO clusters II, for which small values of J_{eff} (40–45 cm^{-1}) have been measured. We therefore must leave open the question of the magnitude of ΔE_{vib}, while still noticing that most of the theoretical studies aimed at analyzing the interplay of J_{Heis}, B, and ΔE_{vib} in [2Fe−2S] clusters have not explicitly included additional static iron site asymmetries (ΔE_{Ω}, ΔE_{solv}, ΔE_{chem}, etc.).

Concerning the g_{av} values, we consistently found that electronic delocalization (small total $\Delta E/B$ ratios) tended to increase the g_{av} value (for plant-type Fd's, $g_{av} = 1.96$) whereas strong trapping forces (large total $\Delta E/B$ ratios) tended to decrease it (for Rieske proteins, $g_{av} = 1.91$). Since the maximum value of 2.03 was obtained for a fully delocalized cluster, the value of 1.96 represents a compromise between the competing trapping (ΔE) and double-exchange (B) terms. This is consistent with the fact that spectroscopic studies have shown that plant-type Fd clusters appear to be valence-trapped.

This intermediate value of 1.96 was shifted downward in the case of one-ligand substitution (Cys → Ser for plant-type clusters). Similarly, the smallest value of 1.91 (for Rieske clusters) was shifted upward upon mutation (His → Cys). Surprisingly, substitution of one ligand was not sufficient to significantly alter the overall $\Delta E/B$ ratio in a drastic way; two such replacements were required (Rieske).

In a parallel way, starting from a common reference of J_{Heis}(rd) ≈ 400 cm^{-1} for both plant-type and Rieske centers, electronic delocalization tended to decrease the effective exchange coupling constant J_{eff} (J_{eff} ≈ 150–200 cm^{-1} for plant-type Fd's), whereas a valence-localized structure tended to maintain a large value (J_{eff} ≈ 380 cm^{-1} for Rieske centers).

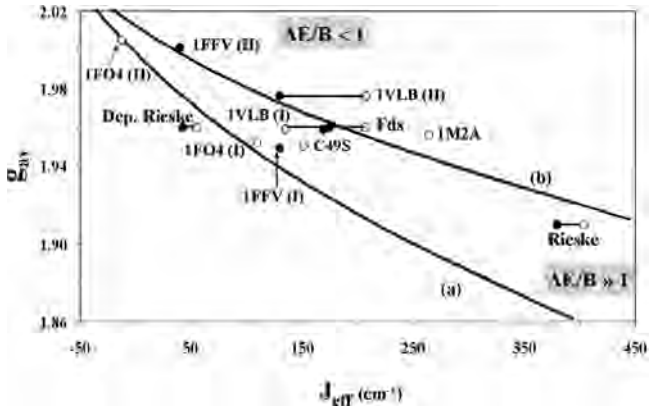

Figure 11. g_{av} as a function of J_{eff}. Symbols: (●) experimental data; (○) computed data. Continuous lines: (a) $g^{BS} = 1.86$; (b) $g^{BS} = 1.92$.

This shows at once a possible correlation between g_{av} and J_{eff} values, which are linked through the variable $\Delta E/B$. As a striking example, for the plant-type Fd's we computed "solvent-free" values of $g_{av} \approx 1.99$ and $J_{eff} \approx 30$ cm^{-1} that became 1.96 and 200 cm^{-1}, respectively, once solvation was included ($\Delta E_{solv}/B \approx 2$), in good agreement with experiment. In Figure 11, we have tentatively plotted J_{eff} as a function of g_{av} for all of the systems encountered in the present study.

In regard to this issue, Salerno et al.[60] observed an empirical relation between J_{eff} and the axial/rhombic character of the EPR signal (measured as $g_2 - g_3$): larger J_{eff} values corresponded to more-axial EPR signals. This first observation was later revisited by Bertrand et al.,[58] who discussed the fact that measured J_{eff} values may strongly depend on the state of the protein (in the intact biological system versus purified or in solution). They supposed, however, that J_{eff} depends solely on the geometry of the bridge. While this is in fact true for J_{Heis}, we have shown that J_{eff} actually contains an additional (ferromagnetic) contribution that depends strongly on solvent accessibility to the cluster (via ΔE_{solv}).

Finally, Bertrand et al.[58] restricted the correlation of Salerno et al.[60] to plant-type Fd's (J_{eff} in the range 150–200 cm^{-1} and $g_2 - g_3 \approx 0.07$–0.09) and to adrenal Fd's ($J_{eff} >$ 340 cm^{-1} and $g_2 - g_3 < 0.05$). On the basis of a combination of crystallographic data and **g**-tensor DFT computations, it has been recently shown how the value of $g_2 - g_3$ is determined by the Fe−Fe−S−C dihedral angles around the Fe#1 reduced site, which range from 120° for rhombic EPR signals to 150° for axial EPR signals. As shown in Figure 4, $\Delta E_\Omega/B$ increased from ~0.5 at 120° to 1.5 at 150°, that is, J_{eff} is expected to increase with dihedral angle (see Figure 3). We thus recovered Bertrand et al.'s empirical correlation between $g_2 - g_3$ and J_{eff}.

The sulfur lone pair arrangement around the [2Fe−2S](Cys)$_4$ cluster (i.e., the ΔE_Ω term) is crucial for a proper understanding and fine-tuning of the cluster electronic structure, as discussed in the appendix in the Supporting Information. It is also algebraic in that some sets of Fe−Fe−S−C dihedral angles "push" the reducing electron onto the opposite iron site ($\Delta E_\Omega < 0$) (see Figure 4). On the basis of our results, we can classify some of the iron site energies in the following order of increasing stability/decreasing energy ("PT" denotes "plant-type"): E(PT Fe#2) ≥ E(PT Fe#1) ≈ E(Cp/Aa Fe#1) > E(Cp/Aa Fe#2). In plant-type Fd's, the solvent-exposed Fe#1 site was only slightly favored ($\Delta E_\Omega/B \approx 0.5$), moreso after a Cys → Ser mutation (Table 4). In Cp/Aa, the structurally similar Fe#1 site, which is located inside the protein, was significantly higher in energy than the (solvent-exposed) Fe#2 site ($\Delta E_\Omega/B \approx$ 1.5–2.0). In the latter case, the Cys → Ser mutation significantly decreased $\Delta E_\Omega/B$ (Table 10). In the closed (solvent-shielded) conformation, the total $\Delta E/B$ value remained small; the combination of this fact with the reduced J_{Heis} value of 200–250 cm^{-1} originating from the S/O mutation resulted in an $S = {}^9/_2$ ground state. The alternate open (solvent-exposed) conformation yielded an $S = {}^1/_2$ ground spin state (see Figure 10).

The proximity of a [2Fe−2S] cluster to the protein surface is not sufficient to ensure a large solvent trapping effect. The orientation of the Fe−Fe axis is also important, as illustrated in Figure 9, thus explaining the difference between plant-type clusters and XO clusters II. At this level, in the light of what we have proposed above (solvent shielding) for the origin of the mutated Cp/Aa $S = {}^9/_2$ ground state, it would be very interesting to study the effect of Cys → Ser mutations on the spectroscopic (EPR/Mössbauer) properties of XO clusters I and/or II, which are also solvent-shielded (especially the buried cluster I).

Finally, for R14 and XO (1FO4) cluster II, we computed relatively small $\Delta E/B$ ratios and J_{eff} coupling constants, as previously found by Noodleman and Han;[104] both quantities had values intermediate between those of typical plant-type Fd ($S = {}^1/_2$) clusters and closed Cp/Aa ($S = {}^9/_2$) clusters. For XO clusters II, inclusion of antisymmetric exchange terms [a combination of ADM (valence-*localized*) and ADE (valence-*delocalized*) terms] that mix the $S = {}^1/_2$ and $S = {}^3/_2$ spin states resulted in an additional increase in g_{av} of up to 0.03–0.05, modulated by $\Delta E/B$ (as can be seen by comparing the results for the 1FO4 and 1VLB clusters II in Table 9).

The last effect we considered is due to the hydrogen-bonding network surrounding a [2Fe−2S] cluster, stabilizing it and affecting its oxidation−reduction potential. At the level of our present models, we did not find any noticeable effect ($\Delta E_H/B < 0.3$) upon adding one-by-one and, at first, on the same side of the cluster (to maximize the asymmetry), all of the >C$_\alpha$H or >NH groups involved in hydrogen bonding in the *Anabaena* 1CZP structure (data not shown).

The question of electronic localization versus delocalization is a delicate one to approach from a quantitative point of view. We chose to demonstrate computationally some of the effects that are potentially involved using a "bottom-up" type of approach. We also gave preference to general and semiquantitative figures illustrating some of the observed correlations.

There are many ways to improve on our results. First, from an empirical point of view (as for our previous DFT study), more crystallographic structures for reduced [2Fe−2S] clusters are needed, as reduction of the protein active site may significantly change the local Fe−Fe−S−C dihedral angles and therefore $\Delta E_\Omega/B$.

The next logical step to go beyond our model would be to treat the electronic problem using an onion-type model with three layers[115,116] (which would be one sort of "top-down" approach). The first layer would involve precise quantum-mechanical (QM) computations of electronic structures of the [2Fe−2S] clusters and their immediate surroundings (ligands and nearby amino acids, especially those involved in the hydrogen-bonding network). The second layer would include the whole protein matrix (charge distribution and polarizable bonds), allowing for the inclusion of the whole electrostatic environment in the model. Finally, the third layer would comprise the solvent, both explicitly (via water molecules attached to the protein surface) and implicitly (through a dielectric continuum).

The modeling of this third layer is critical. In effect, when trying to computationally estimate the amount of solvent trapping (i.e., the ratio $\Delta E_{solv}/B$) and the resulting extra localization of the reducing electron for a given [2Fe−2S] cluster, great caution must be exerted. In vivo, the accessibility of the cluster to solvent (water molecules) strongly depends on whether the protein functions individually or when associated in complexes or even supercomplexes.[117] Moreover, when the protein is purified in solution, its tendency to form dimers (or more complex structures) depends on salt concentration. With higher concentrations (at which crystals are usually obtained), tetramers can result from the oligomerization of dimers.[96,118] Finally, the $\Delta E_{solv}/B$ ratio depends on the proximity of the cluster to the protein surface, the orientation of the Fe−Fe axis with respect to this surface, the protein local conformation (as in the case of the [2Fe−2S] protein from *A. aeolicus*), and so on. In the present work, we used spectroscopic quantities to estimate the amount of extra electronic localization due to solvation. A QM/MM treatment of the same problem hopefully will open the way to do the reverse, that is, to first estimate the ratio $\Delta E_{solv}/B$ in order to subsequently predict its quantitative impact on spectroscopic parameters. An extension of the present work along these lines is planned through a collaboration.

Abbreviations

Aa, *Aquifex aeolicus*; BS, broken-symmetry; Cp, *Clostridium pasteurianum*; Cys, cysteines/cysteinate; DFT, density functional theory; Fd's, ferredoxins; HiPIP, high-potential iron−sulfur proteins; His, histidine; HOMO, highest occupied molecular orbital; HS, high-spin; LS, low-spin ($S = {}^1/_2$); MO, molecular orbital; nc, not computed; PDB, Protein Data Bank; PT, plant-type; Ser, serine; Tt, *Thermus thermophilus*; WT, wild type; XO, xanthine oxidase.

(115) Sinnecker, S.; Neese, F. *J. Comput. Chem.* **2006**, *27*, 1463.
(116) Noodleman, L.; Lovell, T.; Han, W.-G.; Li, J.; Himo, F. *Chem. Rev.* **2004**, *104*, 459.
(117) Guiral, M.; Tron, P.; Aubert, C.; Gloter, A.; Iobbi-Nivol, C.; Guidici-Orticoni, M.-T. *J. Biol. Chem.* **2005**, *280*, 42004.
(118) Morimoto, K.; Yamashita, E.; Kondou, Y.; Lee, S. J.; Arisaka, F.; Tsukihara, T.; Nakai, M. *J. Mol. Biol.* **2006**, *360*, 117.

Appendix A. Energy Denominators for g Tensors

In order to properly compute **g**-tensor values, we needed a reliable evaluation of the $(E_n - E_0)$ gaps in eqs 17 and 18. Let us first restrict this evaluation to the Rieske $\mathbf{g}_{tot}$ tensors only. It will be demonstrated below that the various Rieske models (with NH_3, imidazole, or histidine ligands on the ferrous side) exhibited little to no variation of the computed g_{av} values. This is due to the fact that the reducing electron is fully localized on the iron site bearing the nitrogen ligands. Moreover, the Rieske proteins presented the smallest experimental g_{av} value (1.91) considered in this study. They therefore served as a common reference to which all of the other systems (Fd's, XOs, Fd or Rieske mutants, model complexes, etc.) that had equal or greater values of g_{av} were compared.

On the DFT theoretical side, we first observed that eqs 17 and 18 combined with the three VBP d−d gaps reported in Table A1 yielded a g_{av} value of ∼1.96 for the Rieske models, which was too high. In order to reach the correct value of ∼1.91, we found that the VBP d−d gaps had to be reduced by a factor of ∼2.

In order to find some justification for such a systematic correction, we first noticed that the d−d gaps $(E_n - E_0)_{Slater}$ computed using the Slater transition-state procedure[119] strongly depended on the percentage of HF exchange mixed into the XC hybrid potential. Figure A1 shows the smallest ($d_{z^2} \rightarrow d_{xy}$) gap on the nitrogen (Fe#1) side computed for the $(Imid)_2[Fe\#1-(S_2)-Fe\#2](SCH_3)_2$ model based on the 1JM1 PDB file. As can be seen, the d−d gap values decreased with increasing percentage of HF exchange mixed into the XC potential, falling from 0.37 eV for the VBP potential (i.e., without HF exchange) to 0.08 eV for the

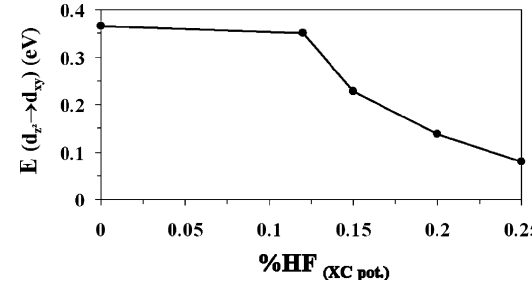

Figure A1. $d_{z^2} \rightarrow d_{xy}$ gaps (eV) as a function of % HF exchange.

Table A1. Comparison of VBP and B3LYP $(E_n - E_0)_{Slater}$ Gaps (eV) for Protonated and Deprotonated Rieske Models Computed Using the Slater Transition-State Procedure

	site #1			site #2		
Rieske model	VBP	B3LYP	%	VBP	B3LYP	%
$(NH_3)_2$ $[Fe\#1-Fe\#2](SH)_2$	0.309	0.119	39	0.453	−	−
	1.118[a]	0.686[a]	163	0.251[a]	0.358[a]	143
$(NH_3)_2$ $[Fe\#1-Fe\#2](SCH_3)_2$	0.335	−	−	0.622	−	−
$(Imid)_2[Fe\#1-Fe\#2]$ $(SCH_3)_2$	0.365	0.138	38	0.290	0.184	63
	0.777[b]	0.394[b]	51	−	−	−
$(Imid\text{-}deprot)_2$ $[Fe\#1-Fe\#2]$ $(SCH_3)_2$	0.200	0.079	40	0.299	0.174	58

[a] $d_{z^2} \rightarrow$ ligand transition. [b] $d_{z^2} \rightarrow d_{xz}$ transition.

Table A2. Heisenberg Exchange Coupling Constants (cm^{-1}) for Oxidized and Reduced Models of Fd's [with $(SH)_4$ and $(SH)_3(OH)$ Ligands], Rieske Centers [with $(SH)_2(NH_3)_2$ and $(SH)_3(NH_3)$ Ligands], and the Doubly Substituted Combination $(SH)_2(OH)_2$

	$(SH)_4$		$(SH)_3(NH_3)$		$(SH)_2(NH_3)_2$		$(SH)_3(OH)$		$(SH)_2(OH)_2$	
	VBP	B3LYP	VBP	B3LYP	VBP	B3LYP	VBP	B3LYP	VBP	B3LYP
$J_{Heis}(ox)$	705	408	746	429	773	411	688	375	671	378
$E_n - E_0$	3420	3140	3944	2694	4202	3517	4234	2944	4642	2960
B	342	(314)	384	188	374	(132)	403	(234)	399	(160)
$\Delta E(HS)$	0	(0)	460	965	959	(1631)	643	(893)	1187	(1245)
$J_{Heis}(rd)$	545	411	637	405	655	432	573	323[a]	545	334[a]

[a] For these C_{2v} dimers, it should be noted that the favored reduced iron site is the one bearing the two SH ligands.

B1LYP potential (with 25% HF exchange). The intermediate B3LYP value (0.14 eV) represented about 40% of the VBP value.

More generally, we compared excitation energies computed for the "local" (VBP) and "non-local" (B3LYP) XC potentials for the four Rieske models listed in Table A1. The BS method by construction localizes the reducing electron on one of the two iron sides. Since this method was devised with the specific goal of providing local monomer electronic and magnetic properties, we thought that the Rieske models, which exhibit inherent chemical asymmetry and resulting electron localization, were best suited to illustrate the impact of the XC potentials (VBP vs B3LYP) on monomer quantities.

As can be seen in Table A1, the $d_{z^2} \rightarrow d_{xy}$ gaps on the nitrogen (Fe#1) side were reduced by 40% on average, whereas on the sulfur (Fe#2) side, the reduction factor was 60%. Moreover, in one instance we were able to compute the next ($d_{z^2} \rightarrow d_{xz}$) energy gap for both XC potentials, this time with a B3LYP/VBP ratio of 51%. Finally, as expected, the few metal → ligand gaps we obtained were larger with B3LYP than with VBP, but they were not the focus of this study as their contribution to g_{av} is minor.

We also tried to compute various metal−metal and metal–ligand transitions for the oxidized BS state of the $(NH_3)_2[Fe_2S_2](SMe)_2$ model using the time-dependent DFT (TDDFT) method with the VBP potential (in the ADF code, the TDDFT procedure is only implemented for systems having an even total number of electrons). As can be seen in Figure S8 in the Supporting Information, the Slater and TDDFT gaps were linearly correlated. The best fits were given by $(E_n - E_0)_{TDDFT} \approx 1.169(E_n - E_0)_{Slater} - 0.130$ or $(E_n - E_0)_{Slater} \approx 0.814(E_n - E_0)_{TDDFT} + 0.146$. However, the TDDFT method did not provide us with small enough gaps.

To conclude this analysis, we verified for all of the cluster models (except for the one $d_{z^2} \rightarrow d_{xz}$ case mentioned above) that with ADF2006, only the first d−d gap (either metal → metal or metal → ligand) was accessible through the Slater transition procedure for the B3LYP hybrid potential, whereas all of these gaps can usually be computed when using a standard (i.e., nonhybrid) XC potential (such as VBP).

Finally, in Table A2 we have presented Heisenberg exchange coupling constants J_{Heis} for oxidized and reduced models of Fd's [with $(SH)_4$ and $(SH)_3(OH)$ ligands], Rieske centers [with $(SH)_2(NH_3)_2$ and $(SH)_3(NH_3)$ ligands], and the doubly substituted combination $(SH)_2(OH)_2$. Only for these small dimers could we converge Slater transition states for the HS ($S = {}^9/_2$) spin states. This allowed us to compare these $(E_n - E_0)_{Slater}$ gaps for the two XC potentials (VBP and B3LYP). For more complicated molecules and models, we systematically computed the Slater gaps at the VBP level and scaled them down by appropriate proportionality coefficients (extracted from Table A2) in order to estimate the corresponding B3LYP gaps.

Appendix B. Antisymmetric Superexchange versus Double-Exchange Hamiltonians

We consider only the two lowest (+) eigenfunctions $\Psi_+({}^1/_2, M_S) = c_a({}^1/_2)\Psi_a({}^1/_2, M_S) + c_b({}^1/_2)\Psi_b({}^1/_2, M_S)$ (with $M_S = \pm{}^1/_2$) and $\Psi_+({}^3/_2, M_S) = c_a({}^3/_2)\Psi_a({}^3/_2, M_S) + c_b({}^3/_2)\Psi_b({}^3/_2, M_S)$ (with $M_S = \pm{}^1/_2, \pm{}^3/_2$) (see eqs 2 and 3). All of the required matrix elements between localized Heisenberg states are given in refs 108–112. We neglect here all ZFS terms (see ref 120 for a treatment including ZFS terms but not ADM/ADE terms).

Within the $\{\Psi_+({}^1/_2, {}^1/_2), \Psi_+({}^3/_2, {}^3/_2), \Psi_+({}^3/_2, -{}^1/_2)\}$ basis, and with the vectors $\mathbf{K}_{AB}$ and $\mathbf{d}_{AB}$ oriented along the x axis (along the sulfur atoms of the S−S bridge), we obtain the following matrix elements:

	$\Psi_+({}^1/_2, {}^1/_2)$	$\Psi_+({}^3/_2, {}^3/_2)$	$\Psi_+({}^3/_2, -{}^1/_2)$
$\Psi_+({}^1/_2, {}^1/_2)$	0	$+iP$	$-iQ$
$\Psi_+({}^3/_2, {}^3/_2)$	$-iP$	${}^3/_2 J_{eff}$	0
$\Psi_+({}^3/_2, -{}^1/_2)$	$+iQ$	0	${}^3/_2 J_{eff}$

where

$$Q = \frac{K_{ABx}\sqrt{14}}{15}[c_a({}^3/_2)c_b({}^1/_2) + c_a({}^1/_2)c_b({}^3/_2)] - \frac{d_{ABx}\sqrt{14}}{4}[c_a({}^1/_2)c_a({}^3/_2) + c_b({}^1/_2)c_b({}^3/_2)] \quad \text{(B1)}$$

and $P = \sqrt{3}Q$. In the limit of full electronic localization, $Q = -d_{ABx}\sqrt{14}/4$, whereas in the case of full electronic delocalization, $Q = (K_{ABx} - d_{ABx})\sqrt{14}/15$. Solving the determinant, we obtain (to first order) a stabilization of the initial doublet state by an amount $-8Q^2/(3J_{eff})$, whereas the degenerate $S = {}^3/_2$ quartet functions, initially placed ${}^3/_2 J_{eff}$ above the doublet state, split into two levels with energies ${}^3/_2 J_{eff}$ and ${}^3/_2 J_{eff} + 8Q^2/(3J_{eff})$. If we now focus on the ground state, the Kramers doublet states (Ψ_+, Ψ_+*) are expressed as

(119) Slater, J. C. *Adv. Quantum Chem.* **1972**, *6*, 1.

(120) Guigliarelli, B.; Bertrand, P.; Gayda, J.-P. *J. Chem. Phys.* **1986**, *85*, 1689.

$$\Psi_+(^1/_2, ^1/_2) \rightarrow \left(1 + \frac{8Q^2}{9J_{\text{eff}}^2}\right)\Psi_+(^1/_2, ^1/_2) + \frac{2iP}{3J_{\text{eff}}}\Psi_+(^3/_2, ^3/_2) - \frac{2iQ}{3J_{\text{eff}}}\Psi_+(^3/_2, -^1/_2)$$

$$\Psi_+(^1/_2, ^1/_2)^* \rightarrow \left(1 + \frac{8Q^2}{9J_{\text{eff}}^2}\right)\Psi_+(^1/_2, -^1/_2)^* - \frac{2iP}{3J_{\text{eff}}}\Psi_+(^3/_2, -^3/_2) + \frac{2iQ}{3J_{\text{eff}}}\Psi_+(^3/_2, ^1/_2) \quad \text{(B2)}$$

following Griffith's convention $\Psi(S, M_S)^* = (-1)^{S-M_S}\Psi(S, -M_S)$ (whereas the coefficients are complex conjugates). We then compute the matrix elements of $\hat{\mathbf{L}} + g_e\hat{\mathbf{S}}$ on the Kramers doublet basis set and finally arrive at the following expression for the average **g**-tensor value g_{av}:

$$g_{\text{av}} \approx g_{\text{av}}(^1/_2)\left(1 + \frac{16Q^2}{9J_{\text{eff}}^2}\right) + g_{\text{av}}(^3/_2)\left(\frac{16Q^2}{27J_{\text{eff}}^2}\right) \quad \text{(B3)}$$

or

$$\Delta g_{\text{av}} = g_{\text{av}} - g_{\text{av}}(^1/_2) \approx \left(\frac{16Q^2}{9J_{\text{eff}}^2}\right)\left[g_{\text{av}}(^1/_2) + \frac{g_{\text{av}}(^3/_2)}{3}\right] \quad \text{(B4)}$$

where $g_{\text{av}}(^1/_2)$ is the g_{av} value for the $S = ^1/_2$ spin state before introduction of any antisymmetric terms. In the case of full electronic localization, $g_{\text{av}}(^1/_2) = ^7/_3 g_{\text{av}}(Fe^{3+}) - ^4/_3 g_{\text{av}}(Fe^{2+}) \approx 1.91$–$1.96$ [with $g_{\text{av}}(Fe^{3+}) \approx 2.02$, this implies $g_{\text{av}}(Fe^{2+}) \approx 2.06$–$2.10$] and $g_{\text{av}}(^3/_2) = ^{13}/_{15} g_{\text{av}}(Fe^{3+}) + ^2/_{15} g_{\text{av}}(Fe^{2+})$ (an average value of 2.03). For $\Delta g_{\text{av}} = 0.05$ and $J_{\text{eff}} = 40$ cm^{-1}, we obtain $Q \approx 4$ cm^{-1}.

With only the ADM mechanism, $Q^2 \approx ^{14}/_{16} d_{ABx}^2$. For $J_{\text{eff}} \approx 40$ cm^{-1} and $\Delta g_{\text{av}} \approx 0.05$, we obtain $d_{ABx} \approx 4.5$ cm^{-1}, which is in fair agreement with the value of de Oliveira et al.[56] ($\sim$8 cm^{-1}) and our value ($\sim$5 cm^{-1}).

On the other hand, Belinsky[108–112] has shown that the ADE mechanism, when present, usually dominates over the ADM term, as $(K_{ABx}/d_{ABx}) \approx -(5B/J_{\text{eff}})$. Neglecting d_{ABx} over K_{ABx} (i.e., ascribing the relaxation effects observed for XO clusters II and R14 only to the ADE mechanism), we obtain $Q^2 = ^{14}/_{225} K_{ABx}^2$, that is, $K_{ABx} \approx 16$ cm^{-1} (Belinsky found 60–100 cm^{-1}). In this limit, $d_{ABx} \approx (J_{\text{eff}}/5B)K_{ABx} \approx 0.2$ cm^{-1} for $B \approx 700$ cm^{-1}.

Belinsky's estimate is larger than ours, even with $B \approx 700$ cm^{-1} (Belinsky assumed 800 cm^{-1} $< B <$ 1350 cm^{-1}). Belinky's expression is actually $K_{ABx} \approx 10B\Delta g_\perp \theta$, where $\Delta g_\perp$ stands for the perpendicular $g_\perp - g_e$ component (proposed to be 0.08) and θ denotes the tilt angle of the two otherwise-idealized [FeS_4] tetrahedra around the common S−S bridging edge (assumed to be 0.1 rad, i.e., 6°). Such a small angle breaking the mirror-plane symmetry between the two iron sites is difficult to estimate for actual (i.e., nonidealized) cluster structures. Moreover, we have already seen how the ligand orientations are crucially important for the determination of the local ferrous ion electronic structure. Therefore, at this level, we cannot say more at the moment.

Finally, it can be easily verified that as an order of magnitude estimate only, $d_{ABx} \approx (J_{\text{eff}}/2)\Delta g_{\text{av}}^{1/2}$ (ADM only) or $K_{ABx} \approx J_{\text{eff}}(3\Delta g_{\text{av}})^{1/2}$ (ADE only); "reality" lies somewhere in between.

Supporting Information Available: Figures S1−S8, eqs S1, Tables S1 and S2, and an appendix discussing the evaluation of vibronic coupling. This material is available free of charge via the Internet at http://pubs.acs.org.

IC701730H